Resource

Cell Reports

Mutant *IDH1* Promotes Glioma Formation *In Vivo*

Graphical Abstract

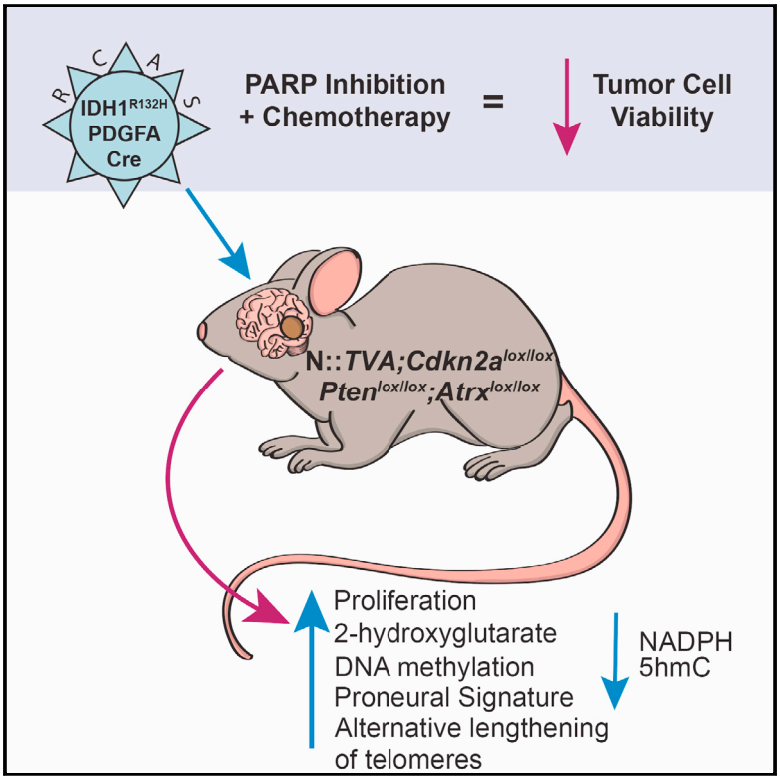

Authors

Beatrice Philip, Diana X. Yu, Mark R. Silvis, ..., Ryan E. Looper, Howard Colman, Sheri L. Holmen

Correspondence

sheri.holmen@hci.utah.edu

In Brief

Philip et al. show that mutant IDH1 cooperates with PDGFA and loss of *Cdkn2a*, *Atrx*, and *Pten* to promote gliomagenesis *in vivo* in a mouse model of glioma. These tumors resemble proneural human mutant IDH1 glioblastoma and exhibit enhanced sensitivity to PARP inhibition in combination with chemotherapy.

Highlights

- IDH1^{R132H} and PDGFA cooperate with loss of *Cdkn2a*, *Atrx*, and *Pten* in gliomagenesis
- 2-HG mediates the oncogenic effects of IDH1^{R132H}
- IDH1^{R132H}-driven tumors mimic the human disease and resemble the proneural subtype
- IDH1^{R132H} tumor cells have enhanced sensitivity to PARP inhibitors

Data and Software Availability

GSE107616

Philip et al., 2018, Cell Reports *23*, 1553–1564
May 1, 2018
https://doi.org/10.1016/j.celrep.2018.03.133

CellPress

Cell Reports
Resource

Mutant *IDH1* Promotes Glioma Formation *In Vivo*

Beatrice Philip,[1,2] Diana X. Yu,[1,2] Mark R. Silvis,[1,2] Clifford H. Shin,[1,3] James P. Robinson,[4] Gemma L. Robinson,[1,2] Adam E. Welker,[1] Stephanie N. Angel,[1,2] Sheryl R. Tripp,[5] Joshua A. Sonnen,[5,6] Matthew W. VanBrocklin,[1,2,3] Richard J. Gibbons,[7] Ryan E. Looper,[8] Howard Colman,[1,9] and Sheri L. Holmen[1,2,3,10,*]

[1]Huntsman Cancer Institute, University of Utah Health Sciences Center, Salt Lake City, UT 84112, USA
[2]Department of Surgery, University of Utah Health Sciences Center, Salt Lake City, UT 84112, USA
[3]Department of Oncological Sciences, University of Utah Health Sciences Center, Salt Lake City, UT 84112, USA
[4]Hormel Institute, University of Minnesota, 801 16th Avenue NE, Austin, MN 55912, USA
[5]ARUP Institute for Clinical and Experimental Pathology, Salt Lake City, UT 84108, USA
[6]Department of Pathology, University of Utah Health Sciences Center, Salt Lake City, UT 84112, USA
[7]MRC Molecular Haematology Unit, Weatherall Institute of Molecular Medicine, University of Oxford, Oxford, UK
[8]Department of Chemistry, University of Utah, Salt Lake City, UT 84112, USA
[9]Department of Neurosurgery, University of Utah Health Sciences Center, Salt Lake City, UT 84112, USA
[10]Lead Contact
*Correspondence: sheri.holmen@hci.utah.edu
https://doi.org/10.1016/j.celrep.2018.03.133

SUMMARY

Isocitrate dehydrogenase 1 (IDH1) is the most commonly mutated gene in grade II–III glioma and secondary glioblastoma (GBM). A causal role for IDH1^{R132H} in gliomagenesis has been proposed, but functional validation *in vivo* has not been demonstrated. In this study, we assessed the role of IDH1^{R132H} in glioma development in the context of clinically relevant cooperating genetic alterations *in vitro* and *in vivo*. Immortal astrocytes expressing IDH1^{R132H} exhibited elevated (R)-2-hydroxyglutarate levels, reduced NADPH, increased proliferation, and anchorage-independent growth. Although not sufficient on its own, IDH1^{R132H} cooperated with PDGFA and loss of *Cdkn2a*, *Atrx*, and *Pten* to promote glioma development *in vivo*. These tumors resembled proneural human mutant IDH1 GBM genetically, histologically, and functionally. Our findings support the hypothesis that IDH1^{R132H} promotes glioma development. This model enhances our understanding of the biology of IDH1^{R132H}-driven gliomas and facilitates testing of therapeutic strategies designed to combat this deadly disease.

INTRODUCTION

Gliomas are the most common primary CNS malignancy, but the molecular mechanisms responsible for their development and progression are not fully understood. In 2008, high-throughput sequencing of World Health Organization (WHO) grade IV glioblastoma multiforme (GBM) tumors identified a novel mutation at codon 132 (R132) in *isocitrate dehydrogenase 1* (*IDH1*) in 12% of the samples analyzed (Parsons et al., 2008). Further studies have found this mutation, or an analogous mutation at codon 172 (R172) in *isocitrate dehydrogenase 2* (*IDH2*), to be present in ~80% of WHO grade II–III gliomas and secondary GBM (Yan et al., 2009b). This mutation had never before been linked to cancer and the mechanism(s) by which it promotes tumor development is under intense investigation. Subsequent studies have identified *IDH* mutations in acute myelogenous leukemia (AML), cholangiocarcinoma, cartilaginous tumors, prostate cancer, papillary breast carcinoma, melanoma, acute lymphoblastic leukemia, angioimmunoblastic T cell lymphoma, and primary myelofibrosis indicating that these genes may be important players in multiple tumor types (reviewed in Cohen et al., 2013).

IDH1 and IDH2 form homodimers in the cytosol and mitochondria, respectively. Dimeric IDH contains two active sites, each composed of amino acid residues from both subunits. Thus, dimerization is essential for its enzymatic activity (Xu et al., 2004). IDH proteins catalyze the oxidative decarboxylation of isocitrate to α-ketoglutarate (α-KG) in a two-step reaction that generates reduced nicotinamide adenine dinucleotide phosphate (NADPH) from $NADP^+$. The IDH1 R132 and IDH2 R172 residues are located in the active sites of the enzyme and are critical for isocitrate binding (Parsons et al., 2008). Mutated IDH proteins utilize NADPH to reduce α-KG to R(–)-2-hydroxyglutarate (2-HG), which is supported by findings that 2-HG levels are elevated in mutant IDH1 gliomas (Dang et al., 2009). Thus, mutant IDH lowers the bioavailability of α-KG, while increased 2-HG competitively inhibits α-KG-dependent dioxygenases, including histone demethylases and the TET family of 5-methylcytosine (5mC) hydroxylases, which mediate DNA demethylation (Xu et al., 2011). As a result, gliomas harboring mutant IDH manifest a glioma-CpG island methylator phenotype (G-CIMP), which epigenetically alters the expression of numerous genes through DNA hypermethylation (Noushmehr et al., 2010).

Recent genomic analysis of diffuse, low-grade gliomas (LGGs) (WHO grades II or III) identified three subclasses consisting of wild-type *IDH* and mutant *IDH* with, or without, 1p/19q co-deletion (Brat et al., 2015). *IDH* mutation appears to be an early event in glioma development due to its presence in lower grade tumors. Nearly 90% of LGGs with an *IDH* mutation but no 1p/19q co-deletion also contained *TP53* mutations and inactivating

alterations of *Alpha Thalassemia/Mental Retardation Syndrome X-Linked* (*ATRX*). Amplification of loci encoding *Platelet-Derived Growth Factor Receptor A* (*PDGFRA*), *Cyclin Dependent Kinase 4* (*CDK4*), and *MYC* was also reported (Brat et al., 2015). These alterations are similar to those observed in the proneural GBM subclass (Verhaak et al., 2010). We and others have further defined these subclasses based on copy number alterations. The *IDH* mutation subclass without 1p/19q co-deletion includes loss of 9p and 10q as well as gain of chromosomes 7 and 12q. Genes at these loci include *Cyclin Dependent Kinase Inhibitor 2A* (*CDKN2A*; 9p21.3), *Phosphatase and Tensin Homolog Deleted on Chromosome Ten* (*PTEN*; 10q23), *Platelet-Derived Growth Factor Alpha* (*PDGFA*; 7q11.23), *CDK4* (12q13), and *Mouse Double Minute 2 Homolog* (*MDM2*; 12q15) (Cimino et al., 2017). Furthermore, we observed that progression of lower grade mutant IDH gliomas to GBM was associated with loss of chromosomal regions surrounding *PTEN* (Cohen et al., 2015).

Functional validation of these alterations in gliomagenesis has been hampered by difficulties establishing glioma mouse models (reviewed in Lenting et al., 2017). Expression of a conditional knockin allele of mutant *IDH1* using Nestin-*Cre* was perinatal lethal in all mice, while expression of mutant *IDH1* using GFAP-*Cre* was perinatal lethal in 92% of mice; no gliomas were observed in surviving mice (Sasaki et al., 2012). Restricted expression of IDH1^{R132H} to the subventricular zone (SVZ) in adult mice using tamoxifen-inducible Nestin-Cre$^{ER(T2)}$ resulted in reduced α-KG, increased 2-HG and DNA methylation, enhanced proliferation of SVZ cells, and infiltration of neuronal and glial progenitor cells into neighboring regions. However, no gliomas were observed in these mice, which suggests that expression of mutant IDH1 alone is insufficient for glioma development (Bardella et al., 2016).

In this study, we delivered mutant *IDH1* postnatally to nestin-expressing cells using the established RCAS/TVA glioma model. IDH1^{R132H} cooperated with PDGFA and loss of *Cdkn2a*, *Atrx*, and *Pten* to transform immortal astrocytes *in vitro* and promote glioma development *in vivo*. Our findings functionally validate the role of IDH1^{R132H} in driving glioma formation.

RESULTS

IDH1^{R132H} Promotes Astrocyte Growth

To evaluate the role(s) of specific genes in glioma development, we and others have used an established mouse model system based on the RCAS/TVA retroviral vector system to induce malignant gliomas *in vivo* (Holland, 2000). Using this somatic-cell gene delivery method, we initially assessed the effect of IDH1^{R132H} expression on the growth of primary astrocytes derived from Nestin*::TVA* (N*::TVA*);*Cdkn2a*$^{lox/lox}$ mice. No differences in astrocyte proliferation were observed between cells infected with RCAS-Cre alone or in combination with either RCAS-IDH1 or RCAS-IDH1^{R132H}, despite Cre-mediated loss of *Cdkn2a* and expression of wild-type (WT) or mutant IDH1 (data not shown). Genomic analysis of LGG subgroups shows that 86% of mutant *IDH1* without 1p/19q loss have inactivation of *ATRX*. ATRX is a core component of the chromatin remodeling complex active in the maintenance of telomeres. Loss of ATRX function appears to promote alternative lengthening of telomeres (ALT), which occurs in the absence of telomerase activity and is a potential precursor to genomic instability (Hu et al., 2016). Therefore, we crossed conditional *Atrx* (*Atrx*^{lox}) mice (Garrick et al., 2006) with N*::TVA*;*Cdkn2a*$^{lox/lox}$ mice to generate N*::TVA*;*Cdkn2a*$^{lox/lox}$;*Atrx*$^{lox/lox}$ mice. Primary astrocytes isolated from these mice were infected with RCAS-Cre alone or in combination with either RCAS-IDH1 or RCAS-IDH1^{R132H}, which are both hemagglutinin (HA) tagged to distinguish virally delivered IDH1 expression from endogenous IDH1 (Figure S1A, left panel). While no significant difference in proliferation was observed between uninfected N*::TVA*;*Cdkn2a*$^{lox/lox}$;*Atrx*$^{lox/lox}$ astrocytes compared to astrocytes infected with RCAS-Cre alone, a 1.5-fold increase in proliferation was observed when these astrocytes were infected with both RCAS-Cre and RCAS-IDH1^{R132H} relative to RCAS-Cre alone ($p = 0.004$; Figure S1B).

Flavahan et al. previously demonstrated aberrant *PDGFRA* gene activation in cells harboring mutant IDH as a result of hypermethylation at cohesin and CCCTC-binding factor (CTCF)-binding sites, which disrupted binding of CTCF, a methylation-sensitive insulator protein (Flavahan et al., 2016). In addition, *IDH* mutation clusters from human gliomas frequently include gain of chromosome 7 (Cimino et al., 2017), which contains *platelet-derived growth factor alpha* (*PDGFA*;7q11.23), and we have observed specific upregulation of *Pdgfra* mRNA in the presence of PDGFA expression *in vivo* (Shin et al., 2017). Therefore, we also evaluated the effect of PDGFRA signaling, via PDGFA expression, on the proliferation rate of N*::TVA*;*Cdkn2a*$^{lox/lox}$;*Atrx*$^{lox/lox}$ astrocytes following infection with RCAS-PDGFA and RCAS-Cre alone or in combination with either RCAS-IDH1 or RCAS-IDH1^{R132H} (Figures S1A and S1B). Significant, but modest, differences in proliferation were observed between uninfected N*::TVA*;*Cdkn2a*$^{lox/lox}$;*Atrx*$^{lox/lox}$ astrocytes, cells infected with each virus alone, or cells infected with the combination of RCAS-PDGFA, RCAS-Cre, and RCAS-IDH1^{R132H} ($p < 0.05$; Figure S1B). Because expression of PDGFA only modestly increased cellular proliferation in this context, we crossed N*::TVA*;*Cdkn2a*$^{lox/lox}$;*Atrx*$^{lox/lox}$ mice with conditional *Pten* (*Pten*^{lox}) mice (Zheng et al., 2008) to generate N*::TVA*;*Cdkn2a*$^{lox/lox}$;*Atrx*$^{lox/lox}$;*Pten*$^{lox/lox}$ mice and model loss of chromosome 10q, which we observed associated with progression of lower grade mutant IDH1 gliomas to GBM (Cohen et al., 2015). Primary astrocytes from these mice were infected with RCAS-PDGFA and RCAS-Cre alone or in combination with either RCAS-IDH1 or RCAS-IDH1^{R132H} and expression was confirmed by western blot (Figure S1A, right panel). Significant differences in proliferation were observed between uninfected N*::TVA*;*Cdkn2a*$^{lox/lox}$;*Atrx*$^{lox/lox}$;*Pten*$^{lox/lox}$ astrocytes and astrocytes infected with each virus individually ($p < 0.04$), but a nearly 10-fold increase in proliferation was observed when these cells were infected with the combination of RCAS-PDGFA, RCAS-Cre, and RCAS-IDH1^{R132H} as compared with uninfected astrocytes or astrocytes infected with RCAS-PDGFA, RCAS-Cre, and RCAS-IDH1 ($p < 0.0001$; Figure 1A). These data demonstrate that IDH1^{R132H} promotes the growth of immortal *Cdkn2a*-deficient mouse astrocytes *in vitro*, and this effect is enhanced by expression of PDGFA in combination with loss of *Atrx* and *Pten*.

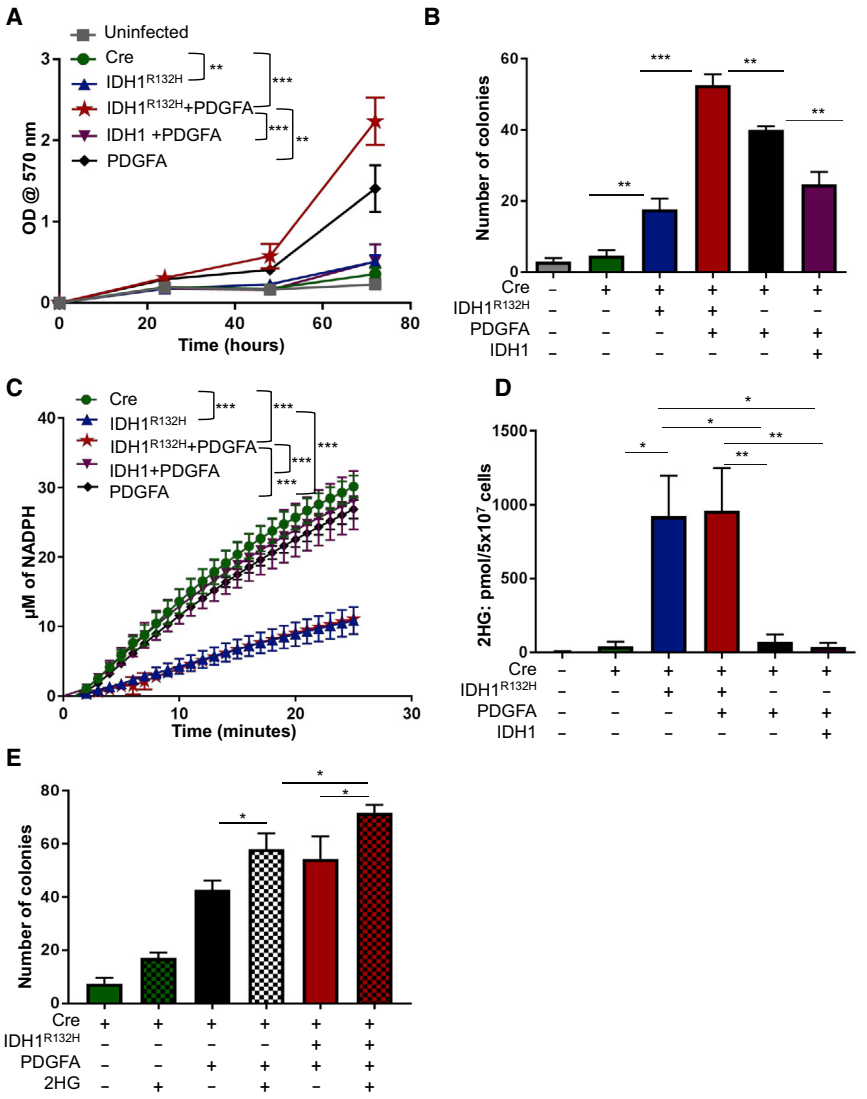

Figure 1. IDH1^{R132H} Promotes Growth of Immortal Astrocytes, Consumes NADPH, and Increases 2-HG Levels

(A) Cell proliferation was determined by MTT assay of astrocytes derived from N::*TVA*;*Cdkn2a*$^{lox/lox}$;*Atrx*$^{lox/lox}$;*Pten*$^{lox/lox}$ mice and infected with viruses containing Cre, IDH1^{R132H}, IDH1, and/or PDGFA as indicated.

(B) Anchorage-independent growth of N::*TVA*;*Cdkn2a*$^{lox/lox}$;*Atrx*$^{lox/lox}$;*Pten*$^{lox/lox}$ astrocytes infected with viruses containing the genes indicated was analyzed by soft agar colony formation assay.

(C) NADPH production was measured from N::*TVA*;*Cdkn2a*$^{lox/lox}$;*Atrx*$^{lox/lox}$;*Pten*$^{lox/lox}$ astrocytes infected with viruses containing the genes indicated.

(D) 2-HG production from N::*TVA*; *Cdkn2a*$^{lox/lox}$;*Atrx*$^{lox/lox}$;*Pten*$^{lox/lox}$ astrocytes infected with viruses containing the genes indicated was detected by LC/MS.

(E) Anchorage-independent growth of N::*TVA*;*Cdkn2a*$^{lox/lox}$;*Atrx*$^{lox/lox}$;*Pten*$^{lox/lox}$ astrocytes infected with viruses containing the genes indicated and/or treated with 2-HG (checked bars) was analyzed by soft agar colony formation assay.

Data are expressed as the mean ± SEM with three replicates. Statistical significance is denoted: *p < 0.05, **p < 0.01, ***p < 0.001. See also Figure S1.

IDH1^{R132H} Promotes Growth in Soft Agar

To evaluate the ability of IDH1^{R132H} to promote anchorage-independent growth, colony formation of N::*TVA*;*Cdkn2a*$^{lox/lox}$;*Atrx*$^{lox/lox}$;*Pten*$^{lox/lox}$ astrocytes was measured in soft agar. We demonstrated previously that astrocytes lacking *Cdkn2a* are immortal in culture but are not transformed as evidenced by their inability to form colonies in the semi-solid soft agar matrix (Robinson et al., 2010). Similarly, very few colonies were detected in astrocytes lacking *Cdkn2a*, *Atrx*, and *Pten* (Figure 1B); however, IDH1^{R132H} expression significantly increased anchorage-independent growth in this context ($p = 0.008$; Figure 1B). Furthermore, PDGFA combined with IDH1^{R132H} expression significantly increased colony number and size, compared with PDGFA expression alone ($p < 0.01$; Figures 1B and S1C). Interestingly, anchorage-independent growth was significantly reduced when WT IDH1 was co-expressed with PDGFA in this context ($p = 0.01$; Figure 1B). Expression of WT IDH1 in immortal astrocytes likely increases cellular levels of α-KG, which has been shown to have anti-tumor activity both *in vitro* and *in vivo* (reviewed in Zdzisińska et al., 2017). These findings demonstrate that mutant IDH1 promotes anchorage-independent growth of immortal *Cdkn2a*-deficient mouse astrocytes *in vitro* in PDGFA-activated cells with loss of *Atrx and Pten.*

IDH1^{R132H} Consumes NADPH and Produces 2-HG

The physiological role of IDH1 is to convert isocitrate to α-KG and produce NADPH (Xu et al., 2004). R132H substitution in IDH1 alters the structure of the enzyme's active site and its enzymatic activity (Parsons et al., 2008). Thus, rather than generating NADPH, IDH1^{R132H} consumes NADPH to generate 2-HG (Dang et al., 2009). To determine the ability of WT IDH1 and IDH1^{R132H} to generate NADPH in N::*TVA*;*Cdkn2a*$^{lox/lox}$;*Atrx*$^{lox/lox}$;*Pten*$^{lox/lox}$ astrocytes, we compared the levels of NADPH produced by these cells following infection with RCAS-Cre and RCAS-IDH1 or RCAS-IDH1^{R132H} in the presence or absence of RCAS-PDGFA. In the presence of isocitrate, cells expressing WT IDH1 generated significantly higher levels of NADPH compared with cells expressing IDH1^{R132H} ($p < 0.001$; Figure 1C). To assess the neomorphic enzymatic activity of IDH1^{R132H}, the level of 2-HG produced in each astrocyte culture expressing IDH1^{R132H} alone, PDGFA alone, PDGFA and IDH1^{R132H}, or PDGFA and WT IDH1 was quantitated using liquid chromatography/mass spectrophotometry (LC/MS). As expected, significantly higher levels of 2-HG were detected in cells expressing IDH1^{R132H} compared

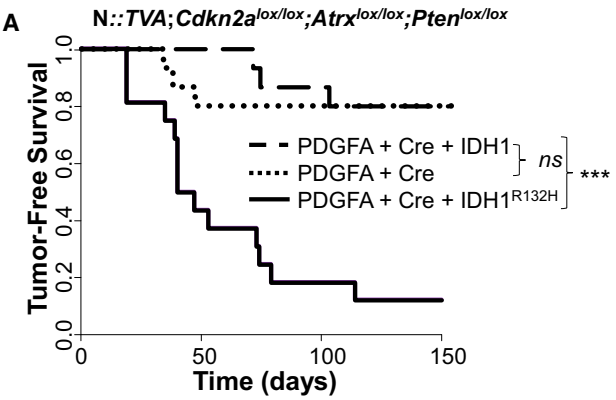

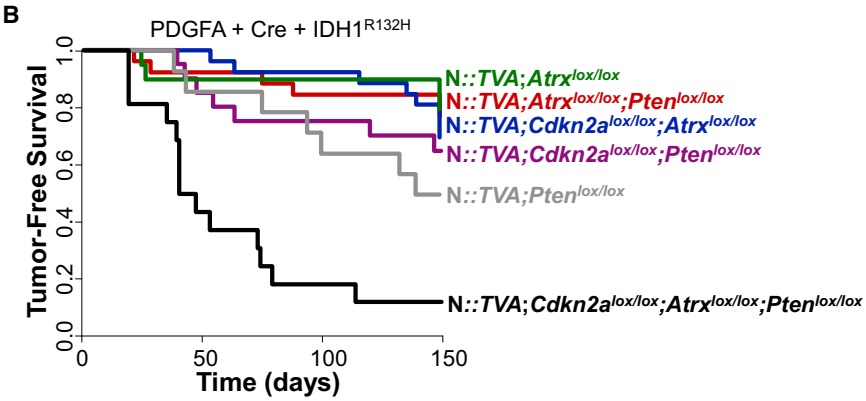

Figure 2. IDH1^{R132H} Cooperates with PDGFA and Loss of *Cdkn2a*, *Atrx*, and *Pten* to Promote Glioma Formation *In Vivo*

(A) Kaplan-Meier tumor-free survival analysis of N::*TVA*;*Cdkn2a*$^{lox/lox}$;*Atrx*$^{lox/lox}$;*Pten*$^{lox/lox}$ mice infected with viruses containing PDGFA and Cre (n = 15, dotted line), PDGFA, Cre, and IDH1 (n = 15, dashed line), or PDGFA, Cre, and IDH1^{R132H} (n = 16, solid line).

(B) Kaplan-Meier tumor-free survival analysis of the mouse strains indicated infected with viruses containing PDGFA, Cre, and IDH1^{R132H}.

Statistical significance is denoted by ***$p < 0.001$. *ns*, not significant. See also Figure S2 and Tables S1 and S2.

with the parental cells regardless of the presence or absence of PDGFA ($p < 0.03$). Astrocytes with IDH1^{R132H} expression produced more than 100-fold greater levels of 2-HG than the parental cells (Figure 1D). In contrast, there was no significant difference in 2-HG levels between cells expressing PDGFA alone or cells expressing PDGFA in combination with WT IDH1 when compared with the parental cells (Figure 1D). These data demonstrate that mouse astrocytes expressing IDH1^{R132H} behave similarly to human glioma cells harboring IDH1^{R132H} with respect to decreased NADPH production and increased levels of 2-HG.

Effects of IDH1^{R132H} Are Mediated by 2-HG

To investigate whether the effects of IDH1^{R132H} in this context are mediated by 2-HG, N::*TVA*;*Cdkn2a*$^{lox/lox}$;*Atrx*$^{lox/lox}$;*Pten*$^{lox/lox}$ astrocytes expressing Cre alone or Cre and PDGFA were suspended in soft agar and treated with vehicle (DMSO) or a cell membrane-permeable [tri-fluoromethyl benzyl (TFMB)-esterified] version of (*R*)-2HG (Losman et al., 2013). Treatment of these cells with TFMB-(*R*)-2HG significantly enhanced anchorage-independent growth in all cells analyzed relative to their vehicle-treated controls. In cells expressing PDGFA and Cre, addition of TFMB-(*R*)-2HG mimicked the anchorage-independent growth observed in cells expressing IDH1^{R132H}. Interestingly, TFMB-(*R*)-2HG further enhanced colony formation in cells expressing IDH1^{R132H} (Figure 1E). These data suggest that the effects of IDH1^{R132H} on anchorage-independent growth are mediated by 2-HG.

IDH1^{R132H} Promotes Glioma Formation *In Vivo*

Previous studies have demonstrated that IDH1^{R132H} expression alone is insufficient to initiate glioma development in mice (Amankulor et al., 2017; Bardella et al., 2016), and our data support these findings. Informed by our *in vitro* studies, we evaluated the effect of IDH1^{R132H} expression in cooperation with additional genetic alterations *in vivo*. While intracranial delivery of RCAS-Cre and RCAS-IDH1^{R132H} in combination did not result in glioma development or a decrease in survival within the experimental time frame of 150 days in N::*TVA*;*Cdkn2a*$^{lox/lox}$;*Atrx*$^{lox/lox}$;*Pten*$^{lox/lox}$ mice (Table S1), the addition of RCAS-PDGFA led to glioma development in 88% (14/16) of injected mice in this context (Figure 2; Tables S1 and S2). Median survival was 43.5 ± 11 days in this cohort. In contrast, intracranial delivery of RCAS-Cre and RCAS-PDGFA with or without RCAS-IDH1 into N::*TVA*;*Cdkn2a*$^{lox/lox}$;*Atrx*$^{lox/lox}$;*Pten*$^{lox/lox}$ mice resulted in tumor development in only 20% (3/15) of injected mice for both conditions. The difference between either of these cohorts and the mutant IDH1 cohort is highly significant ($p = 3.8 \times 10^{-5}$; and 4.0×10^{-4}, respectively; Figure 2A). A significant difference in tumor incidence and median survival was also observed between N::*TVA*;*Cdkn2a*$^{lox/lox}$;*Atrx*$^{lox/lox}$;*Pten*$^{lox/lox}$ mice and all other strains of mice evaluated (N::*TVA*;*Atrx*$^{lox/lox}$, N::*TVA*;*Atrx*$^{lox/lox}$;*Pten*$^{lox/lox}$, N::*TVA*;*Cdkn2a*$^{lox/lox}$;*Atrx*$^{lox/lox}$, N::*TVACdkn2a*$^{lox/lox}$;*Pten*$^{lox/lox}$ and N::*TVA*; *Pten*$^{ox/lox}$) injected with RCAS-PDGFA, RCAS-Cre, and RCAS-IDH1^{R132H} ($p < 0.0001$) (Figures 2B and S2; Tables S1 and S2). This demonstrates the significant cooperativity and necessity of these combined genetic alterations in promoting tumor development and demonstrates that IDH1^{R132H} promotes glioma formation in this context.

Brain sections from all mice were examined following necropsy and were scored by a board-certified neuropathologist (J.A.S.) as "no tumor," "low-grade tumor," or "high-grade tumor" based on histological features apparent in H&E-stained sections. Low-grade tumors demonstrated single cell infiltration

with nuclear atypia including hyperchromasia and pleomorphism, while high-grade tumors also exhibited mitotic figures, vascular proliferation, and/or areas of pseudopalisading necrosis (Figures 3A and S3). All of the tumors that developed in the N::*TVA*;*Cdkn2a*$^{lox/lox}$;*Atrx*$^{lox/lox}$;*Pten*$^{lox/lox}$ mice were high grade except one tumor in the RCAS-PDGFA and RCAS-Cre cohort. Cre-mediated recombination of *Atrx*, *Cdkn2a*, and *Pten* was assessed by immunohistochemistry (IHC) for ATRX, p19ARF, and PTEN, respectively (Figure S4). The majority of cells in the low-grade tumor in the RCAS-PDGFA and RCAS-Cre cohort continued to express ATRX (data not shown). High-grade tumors were positive for endomucin, an endothelial cell marker, indicating aberrant proliferative vasculature (Figure S4). Virally delivered RCAS-IDH1^{R132H} was detected by IHC with an antibody that specifically detects IDH1^{R132H} and both wild-type and mutant IDH1 were also detected using an antibody that recognizes the HA epitope tag (Figure 3A). All tumors highly expressed PDGFA (Figures 3A and S4) and the oligodendrocyte marker, Olig2, but IHC for the astrocyte marker, glial fibrillary acidic protein (GFAP), appeared to be limited to non-tumorigenic reactive astrocytes (Figure 3A). The high-grade tumors in each cohort were assessed for proliferation by IHC for Ki67 (Figure 3B). The mean percentage of Ki67 positive cells was quantified from three high-powered fields using ImageJ (Almeida et al., 2012). The average percentage of Ki67 positive cells was 21.2% ± 1.5% in the PDGFA and Cre tumors, 27.1% ± 2.3% in the PDGFA, Cre and IDH1 tumors, and 26.2% ± 4.6% in the PDGFA, Cre, and IDH1^{R132H} tumors. No significant difference was observed between any of the pairwise comparisons.

IDH1^{R132H} Gliomas with ATRX Loss Display an ALT Phenotype

ALT is an adaptive mechanism utilized by tumor cells that lack telomerase activity and hence rely on a telomerase-independent mechanism for maintenance of their telomere length (Hu et al., 2016). The ALT phenotype is characterized by the co-localization of the telomeres with ALT-associated promyelocytic leukemia (PML)-like bodies (APBs), which are a subset of PML bodies that are present only in ALT positive and telomerase negative tumors (Draskovic et al., 2009; Jiang et al., 2009). To detect the presence of APBs and their co-existence with telomeres, we performed immuno-FISH with telomere probes and an anti-PML antibody. As expected, *Atrx*-deficient tumors exhibited co-localization of APBs with telomeres, whereas WT *Atrx* tumors did not (Figure 4).

IDH1^{R132H}-Driven Tumors Most Closely Resemble the Proneural Subtype

Human GBM has been classified into four different subtypes consisting of proneural, classical, mesenchymal, and neural (Verhaak et al., 2010). High-grade IDH1^{R132H}-driven tumors in mice resemble human GBM histologically, but it is unclear which subtype, if any, they model. To determine whether the IDH1^{R132H}-driven mouse gliomas resembled a particular subtype, we performed gene expression analysis on RNA extracted from formalin-fixed paraffin-embedded (FFPE) high-grade gliomas generated in N::*TVA*;*Cdkn2a*$^{lox/lox}$;*Atrx*$^{lox/lox}$;*Pten*$^{lox/lox}$ mice by delivery of RCAS-PDGFA, RCAS-Cre, and RCAS-IDH1^{R132H} as well as high-grade gliomas generated with RCAS-PDGFA and RCAS-Cre with RCAS-IDH1 in the same mouse strain. Three tumors from each cohort were analyzed by RNA sequencing. We have previously shown that the transcript coverage and exonic mapping rate we observed are typical for FFPE tissue (Shin et al., 2017). We performed gene set enrichment analysis (GSEA) to compare the expression pattern of these tumors with the datasets from the four GBM subtypes as described previously (Lu et al., 2016). Based on GSEA, the signature gene sets associated with human proneural GBM subtype were significantly enriched in the gene expression profile of IDH1^{R132H}-driven mouse tumors with a significant normalized enrichment score (NES) of 2.11. None of the signature gene sets from any of the other subtypes were significantly associated with the IDH1^{R132H}-driven tumors (Figure 5).

IDH1^{R132H} Alters the Methylation Landscape in Mouse Gliomas

2-HG is a competitive inhibitor of α-KG-dependent dioxygenases including the TET family of 5mC hydroxylases. In human cells, DNA methylation primarily occurs as a 5mC modification of the cytosine bases in CpG dinucleotides. 5mC is an important epigenetic mark that is involved in the control of gene transcription. However, recent studies have identified 5-hydroxymethylcytosine (5hmC), which is formed by oxidation of 5mC by TET enzymes (Tahiliani et al., 2009). Xu et al. demonstrated that mutant IDH1 and IDH2 inhibit 5hmC production by TET (Xu et al., 2011). To assess this phenotype in the tumors that developed in our mouse model, we performed IHC for 5hmC on all tumors that developed in injected N::*TVA*;*Cdkn2a*$^{lox/lox}$;*Atrx*$^{lox/lox}$;*Pten*$^{lox/lox}$ mice. Consistent with decreased activity of TET in cells expressing IDH1^{R132H}, we observed significantly decreased 5hmC staining in IDH1^{R132H} tumors compared with tumors expressing WT IDH1 or PDGFA and Cre alone (Figures 6A and 6B). A modest, but significant, decrease in 5hmC staining was also observed in the WT IDH1 tumors compared to the PDGFA and Cre-only tumors. This may be explained by the finding that wild-type IDH1 can also catalyze the conversion of α-KG to 2-HG, albeit less efficiently than mutant IDH (Pietrak et al., 2011).

Decreased 5hmC levels in IDH1^{R132H} tumors suggested that the mouse tumors exhibit a hypermethylation phenotype similar to what is observed in the human disease. To further validate this finding, the DNA methylomes in the mouse gliomas were profiled using methyl-seq. As an initial analysis to demonstrate the similarity between samples, a clustered heatmap was generated and the sample to sample distance was measured using Euclidean distance (Figure S5A). Differentially methylated CpG regions in both IDH1^{R132H} and IDH1 expressing cells were identified and clustered using K-means algorithm. Expression of mutant IDH1 caused a marked increase in hypermethylation at a large number of CpG regions compared to WT IDH1 (Figures 6 and S5B). Two robust differential DNA methylation clustering patterns, which correlated with IDH1^{R132H} samples with high methylation levels and WT IDH1 with relatively lower methylation levels, were observed (Figure 6). Further analysis of the methylation targets between IDH1^{R132H} and WT IDH1 tumors revealed 16,179 regions that were differentially methylated, including 3,433 differentially methylated CpG regions that intersect within 3 kb

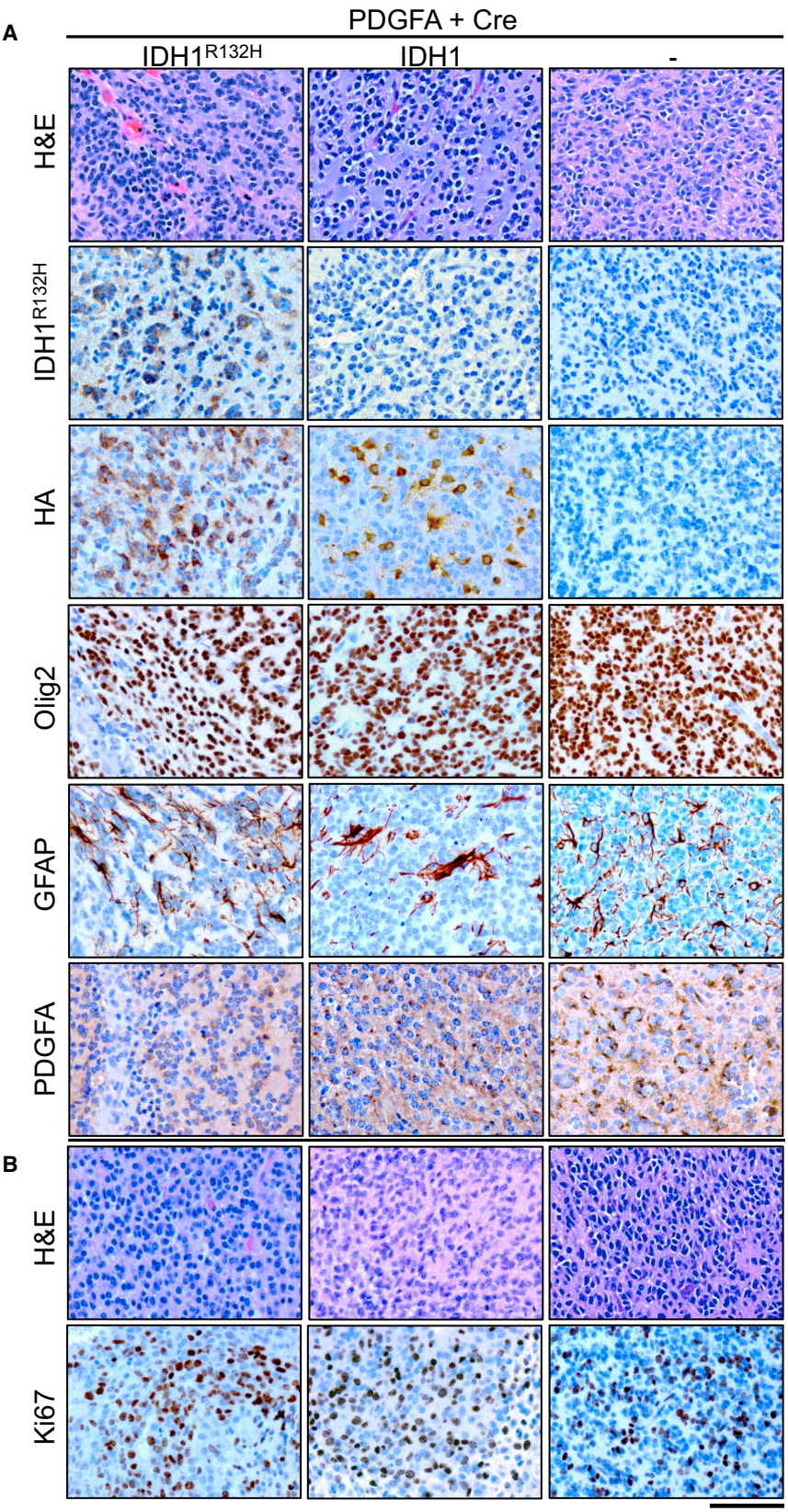

Figure 3. Histological Examination of Gliomas from N::*TVA*;*Cdkn2a*$^{lox/lox}$;*Atrx*$^{lox/lox}$;*Pten*$^{lox/lox}$-Injected Mice

(A) Representative H&E and IHC images for indicated antibodies IDH1^{R132H}, HA, Oligo2, GFAP, and PDGFA for gliomas from each cohort of mice injected with viruses containing PDGFA and Cre alone (right column) or in combination with IDH1^{R132H} (left column) or WT IDH1 (middle column).

(B) Representative high-power H&E and Ki67 images of tumors generated in mice injected with viruses containing PDGFA and Cre alone (right column) or in combination with IDH1^{R132H} (left column) or WT IDH1 (middle column) as indicated. Scale bar represents 100 μm.

See also Figures S3 and S4.

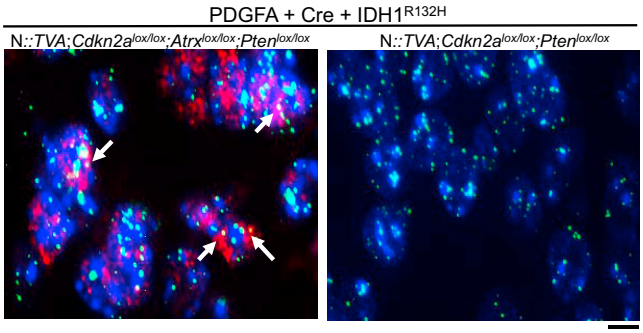

Figure 4. IDH1^{R132H} Gliomas with *Atrx* Loss Display an ALT Phenotype

Representative images of immuno-FISH on brain sections from N::*TVA*;*Cdkn2a*$^{lox/lox}$;*Atrx*$^{lox/lox}$;*Pten*$^{lox/lox}$ and N::*TVA*;*Cdkn2a*$^{lox/lox}$;*Pten*$^{lox/lox}$ gliomas from mice injected with viruses containing PDGFA, Cre, and IDH1^{R132H}. White arrows indicate the co-localization of ALT-associated promyelocytic leukemia-like bodies (red) with telomeres (green). Background nuclear DNA is stained with Hoechst 33342 (blue). Scale bar represents 10 μm.

of a promoter. There were 13,570 regions that were hypermethylated and 2,609 that were hypomethylated in IDH1^{R132H} tumors compared with WT IDH1 tumors.

IDH1^{R132H}-Expressing Cells Demonstrate Enhanced Sensitivity to PARP Inhibitors

Previous studies revealed that IDH1 mutant cells are hypersensitive to poly-(adenosine 5′-diphosphate-ribose) polymerase (PARP) inhibitors (Lu et al., 2017; Sulkowski et al., 2017). This phenotype was further validated by others in glioma cell lines ectopically expressing IDH1^{R132H} (Lu et al., 2017), in primary patient-derived IDH1^{R132H} glioma cells, and in subcutaneous xenograft tumor models (Sulkowski et al., 2017). We assessed the cytotoxicity of the PARP inhibitor, olaparib, alone and in combination with temozolomide (TMZ), a DNA alkylating agent that is currently the standard of care for patients with IDH mutant gliomas, using primary tumor cells derived from IDH1^{R132H} and WT IDH1 gliomas as well as astrocytes from N::*TVA*;*Cdkn2a*$^{lox/lox}$;*Atrx*$^{lox/lox}$;*Pten*$^{lox/lox}$ mice infected with viruses containing PDGFA, Cre, and IDH1^{R132H} or IDH1. We observed enhanced sensitivity to olaparib in cells harboring IDH1^{R132H} compared with WT IDH1. IC_{50} values from dose-response curves of olaparib were 26.6 and 85.3 μM for IDH1^{R132H} astrocytes and tumor cells, respectively (Figure 7A), while the IC_{50} values of their WT counterparts were >100 μM (Figure 7B). Furthermore, TMZ significantly enhanced the cytotoxic effects of olaparib in IDH1^{R132H} cells. Addition of TMZ at 10, 25, and 50 μM potentiated the cytotoxicity of olaparib selectively in IDH1^{R132H}-expressing cells, reducing the olaparib IC_{50} from 26.6 to 23.4 μM, 9.51 μM, and 3.76 μM in astrocytes and from 85.3 to 32.4 μM, and 18.9 to 13.9 μM in tumor cells, respectively (Figure 7A). No significant potentiation was observed in cells expressing WT IDH1 (Figure 7B). In agreement with a previous study that reported enhanced vulnerability of glioma cells ectopically expressing IDH^{R132H} to TMZ (Lu et al., 2017), we also observed sensitivity in astrocytes expressing IDH1^{R132H} (Figure 7C, inset). However, the combination of TMZ and olaparib resulted in a significant reduction in cell viability compared with either agent alone for both astrocytes and tumor cells expressing IDH1^{R132H}, suggesting that this is an effective therapeutic strategy for the treatment of IDH1^{R132H} tumors (Figures 7C and 7D).

DISCUSSION

In this study, we provide *in vivo* evidence that IDH1^{R132H} promotes gliomagenesis. We observed that IDH1^{R132H} cooperates with PDGFA and loss of the tumor suppressors *Cdkn2a*, *Atrx*, and *Pten* to induce tumor development but was not sufficient to promote tumor development on its own. Our findings are consistent with a previous study in which specific expression of IDH1^{R132H} in nestin-expressing cells within the SVZ in adult mice did not produce tumors but led to increased 2-HG, enhanced proliferation, and infiltration of neuronal and glial progenitor cells into neighboring regions (Bardella et al., 2016). Modrek et al. reported similar findings using a human neural stem cell model in the context of mutant *IDH1* with loss of *TP53* and *ATRX* (Modrek et al., 2017). Likewise, Amankulor et al. (2017) did not observe glioma development using the RCAS/TVA glioma model when mutant *IDH1* was expressed alone or in combination with *TP53* loss and/or *Cdkn2a* loss. Gliomas were induced when combined with PDGFA, but there was no significant difference in survival between mice harboring tumors expressing either wild-type or mutant *IDH1* in the context of homozygous *Cdkn2a* loss. Similarly, we did not observe a significant difference in survival between mice harboring tumors expressing either PDGFA alone or in combination with wild-type or mutant *IDH1* in the context of homozygous *Cdkn2a* loss or in combination with *Pten* loss. Our data suggest that loss of all three tumor suppressors *Cdkn2a*, *Atrx*, and *Pten* in combination is necessary for IDH1^{R132H} and PDGFA to significantly enhance tumor penetrance and decrease tumor latency (Figures 2 and S2).

Loss of *Cdkn2a* eliminates expression of INK4A and alternative reading frame (ARF), which function to regulate the retinoblastoma (RB) and TP53 pathways, respectively. In the absence of these cell-cycle checkpoints, cells are able to bypass senescence until their telomeres become critically short and they enter crisis. Loss of *Atrx* enables these cells to use recombination as a mechanism to lengthen their telomeres and escape crisis in the absence of telomerase activation. However, it was recently reported that dysregulation of both the TP53 and RB pathways as well as *ATRX* loss was not sufficient to drive this process in human astrocytes. Interestingly, combined loss of *ATRX* and expression of mutant *IDH1* was required in T53/RB-deficient human astrocytes to produce the ALT phenotype, bypass telomere crisis, and escape cell death (Mukherjee et al., 2018). Nonetheless, this combination was still unable to promote tumor development *in vivo* within the experimental time frame of 150 days (Table S1), which suggests that further cooperating events are required. The PI3K/AKT pathway is one of the most commonly altered signaling pathways in cancer. It is activated by a number of mechanisms including but not limited to signaling from receptor tyrosine kinases (RTK) and loss of the tumor suppressor *PTEN*. Activation of the PI3K/AKT signaling pathway not only promotes cell survival, progression through the cell cycle, and cell migration but

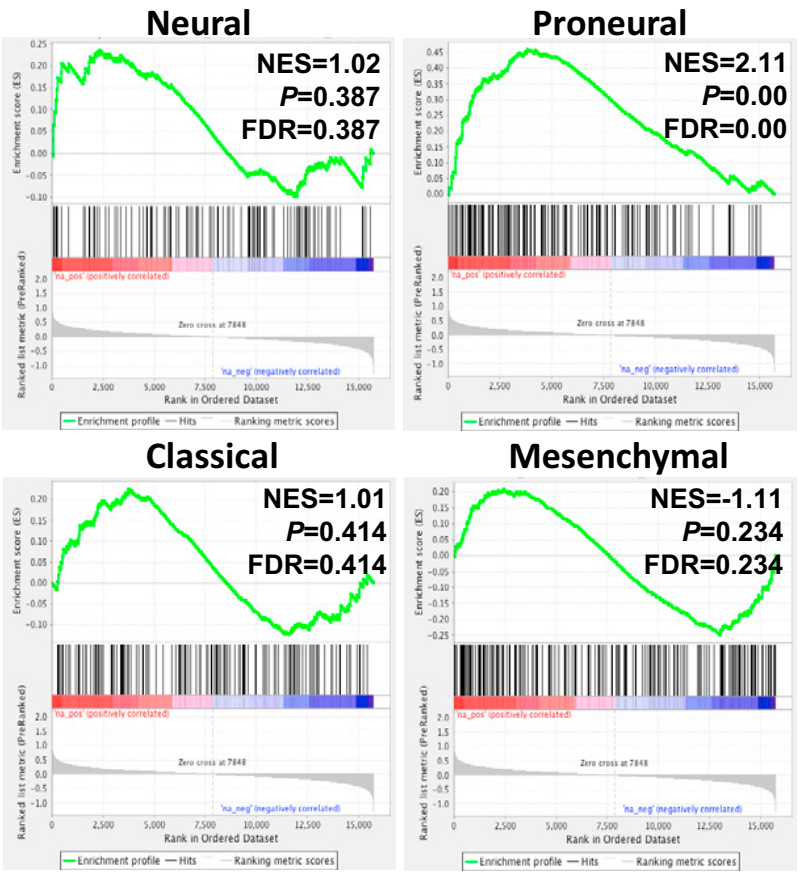

Figure 5. GSEA Comparison between Mouse and Human GBM

GSEA enrichment plots showing the comparison of gene expression profiles in high-grade tumors derived from N::*TVA*;*Cdkn2a*$^{lox/lox}$;*Atrx*$^{lox/lox}$;*Pten*$^{lox/lox}$ mice infected with viruses containing PDGFA, Cre, and IDH1^{R132H} with the TCGA signature gene sets in neural, proneural, classical, and mesenchymal GBM as indicated. NES, normalized enrichment score; p value represents the statistical significance of the enrichment score; FDR, false discovery rate.

also has profound effects on cellular metabolism including up-regulation of glutamine transporters (Boehmer et al., 2003). The ability of mutant IDH1 to produce 2-HG is limited by the availability of its substrate α-KG. To generate 2-HG from α-KG, mutant IDH1 relies on wild-type IDH1 to convert isocitrate to α-KG. This may explain why the wild-type allele is retained and mutant IDH1 is almost always heterozygous. 2-HG has also been shown to be derived from glutamine (Dang et al., 2009). Glutamine enters the cell via transporters and is converted to glutamate by mitochondrial glutaminase. Glutamate can then be converted to α-KG by either glutamate dehydrogenase or by amino-transferases. Activation of PI3K/AKT signaling by PDGFA and loss of PTEN likely leads to increased glutamine uptake, which further cooperates with mutant IDH1 to promote tumorigenesis by providing a source of α-KG for further production of 2-HG. We are currently evaluating this hypothesis.

The mouse tumors resemble high-grade human mutant *IDH1* gliomas genetically, histologically, and functionally. The majority of human *IDH1* mutant gliomas contain inactivating alterations of *ATRX*. Loss of 9p (*CDKN2A*; 9p21.3) and 10q (*PTEN*; 10q23) as well as gain of chromosomes 7 (*PDGFA*; 7q11.23) and 12q (*CDK4*; 12q13 and *MDM2*; 12q15) have also been observed (Cimino et al., 2017). The majority of mutant *IDH1* gliomas also contain *TP53* mutations (94%) (Brat et al., 2015), which was not directly evaluated in this study but is currently under investigation. Deletion of the *Cdkn2a* locus results in loss of the tumor suppressor ARF, which normally regulates TP53 function via MDM2, and loss of the tumor suppressor p16, which normally regulates Rb function via CDK4/6. Therefore, disruption of both the TP53 and Rb pathways was evaluated through deletion of *Cdkn2a*.

Histologically, the mutant *IDH1* mouse tumors were highly proliferative, contained abnormal vasculature, and exhibited areas of pseudopalisading necrosis (Figures 3, S3, and S4). Functionally, mouse astrocytes containing IDH1^{R132H} produced over 100-fold greater levels of 2-HG than the parental cells or cells containing WT IDH1 (Figure 1D). This increase is similar to the fold changes observed in patient tumor samples relative to normal brain tissue (Dang et al., 2009). We also observed the presence of APBs and their co-existence with telomeres in *Atrx*-deficient tumors, which suggests that the mechanism by which these tumor cells bypass crisis as a result of shortened telomeres is through ALT (Figure 4). We and others have previously shown that mouse gliomas driven by PDGFA in the context of *Cdkn2a* and *Pten* loss resemble the proneural subtype of human GBM (Ozawa et al., 2014; Shin et al., 2017). Comparison of the IDH1^{R132H} tumors to the human subtype signatures demonstrated that they positively correlated with the pronerual signature (Figure 5), which is characterized by IDH mutation and alterations in PDGFRA signaling in the human disease (Verhaak et al., 2010). Bardella et al. (2016) performed a similar GSEA of conditional knockin mice induced to express IDH1^{R132H} in SVZ cells at 5 weeks of age and also observed a significant association with the proneural subtype.

The TET family of 5mC hydroxylases, which mediate DNA demethylation (Xu et al., 2011), are inhibited by high 2-HG levels. As a result, gliomas harboring mutant *IDH* manifest a G-CIMP, which epigenetically alters the expression of numerous genes through DNA hypermethylation (Noushmehr et al., 2010). We observed significantly decreased 5hmC staining in IDH1^{R132H} tumors compared with tumors expressing WT IDH1, which is consistent with decreased activity of TET in cells expressing

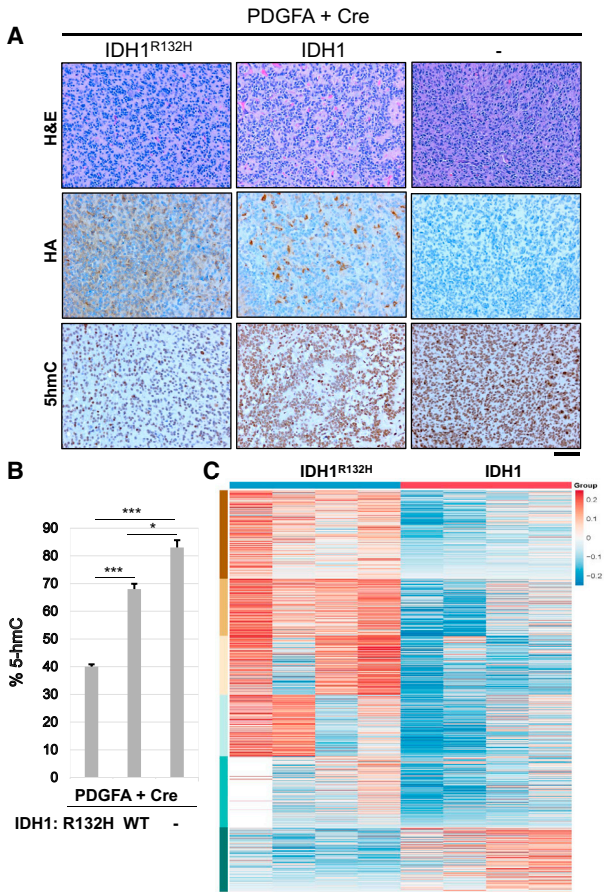

Figure 6. IDH1^{R132H} Reduces 5hmC Levels and Alters the Methylation Landscape in Mouse Gliomas

(A) Representative IHC images of 5hmC expression in gliomas generated in N::*TVA*;*Cdkn2a*$^{lox/lox}$;*Atrx*$^{lox/lox}$;*Pten*$^{lox/lox}$ mice injected with viruses containing PDGFA and Cre alone (right column) or in combination with IDH1^{R132H} (left column) or WT IDH1 (middle column) as indicated. Scale bar represents 100 μm.

(B) Quantification of 5hmC IHC in all three tumor types.

(C) Heatmap comparing the relative difference of the regional fraction methylation of differentially methylated CpG regions between IDH1^{R132H} and IDH1 samples.

Columns correspond to samples and rows correspond to regions organized into 6 groups by k-means algorithm. See also Figure S5.

IDH1^{R132H} (Figures 6A and 6B). Global assessment of DNA methylation in the mouse tumors revealed a large number of differentially methylated CpG regions between IDH1^{R132H} tumors and WT IDH1 tumors (Figures 6C and S5). These observations suggest that IDH1^{R132H} induces a global hypermethylation phenotype in the mouse gliomas similar to the human disease.

In a prospective analysis, grade II–IV glioma patients with mutated *IDH1* or *IDH2* had significantly longer overall survival than patients without *IDH* mutation (Sanson et al., 2009). This finding has been confirmed independently by others (Weller et al., 2009; Yan et al., 2009b). Interestingly, the presence of an *IDH* mutation was found to be an independent marker for better prognosis (Sanson et al., 2009). GBM patients with mutated *IDH1* or *IDH2* have an average survival of 31 versus 15 months for patients without the mutation (Sanson et al., 2009; Yan et al., 2009a). Patients with anaplastic astrocytomas containing *IDH* mutations also had a statistically significant increase in average overall survival when compared with patients without *IDH* mutations (Yan et al., 2009b). These clinical findings suggested that tumors harboring mutations in *IDH* are more sensitive to conventional chemotherapy and radiotherapy, and this was confirmed by two independent clinical studies, but the mechanistic basis for these observation was unclear (Cairncross et al., 2014; Tran et al., 2014). Sulkowski et al. (2017) recently shed light on this mechanism by demonstrating that 2-HG produced by mutant *IDH* induces a defect in homologous recombination (HR), via inhibition of histone lysine demethylases, and reduced ability to repair DNA double-strand breaks. Cancers with defects in DNA repair are often highly sensitive to PARP inhibitors. Therapeutics developed based on this approach have been effective in treating hereditary breast and ovarian cancers, which have defects in BRCA1 and BRCA2, and the Food and Drug Administration (FDA) has approved two PARP inhibitors, rucaparib and olaparib, to treat certain BRCA mutant ovarian cancers. Sulkowski et al. further demonstrated that mutant IDH tumor cells are sensitive to olaparib. We confirmed these findings and demonstrated potentiation of olaparib with the alkylating agent TMZ in both astrocytes and tumor-derived cells lines (Figure 7).

The discovery of mutations in *IDH* has cast a new light on the molecular landscape in glioma and is changing the paradigm for how the disease is defined and treated. Several small molecule inhibitors targeting mutant IDH have been generated and are in various stages of development (Dang et al., 2016). A selective inhibitor of mutant IDH1 inhibited the production of 2-HG and the growth of cells expressing IDH1^{R132H}, but this was independent of its epigenetic effects (Rohle et al., 2013). Demonstration of *in vivo* efficacy of these and other therapies in a relevant glioma model would further support translation to the clinic. The model we described in this study will aid in furthering our understanding of the biology of mutant *IDH1* gliomas and is ideally suited for assessing rational therapeutic strategies designed to combat this deadly disease.

EXPERIMENTAL PROCEDURES

Further details and an outline of resources used in this work can be found in Supplemental Experimental Procedures.

Statistical Methods

Survival data analysis was performed using a log-rank test of the Kaplan-Meier estimate of survival. Cell proliferation and NADPH assay p values were determined by two-way ANOVA (*p < 0. 05, **p < 0. 01, ***p < 0. 001). To compare means, two-tailed Student's t test was used. Ki67-stained cells were quantitated using ImageJ software as described (Almeida et al., 2012). p values below 0.05 were considered significant.

Mice

N::*TVA*;*Cdkn2a*$^{lox/lox}$;*Atrx*$^{lox/lox}$;*Pten*$^{lox/lox}$ mice were produced by crossing pre-existing strains. All experimental procedures were approved by the Institutional Animal Care and Use Committee (IACUC) at the University of

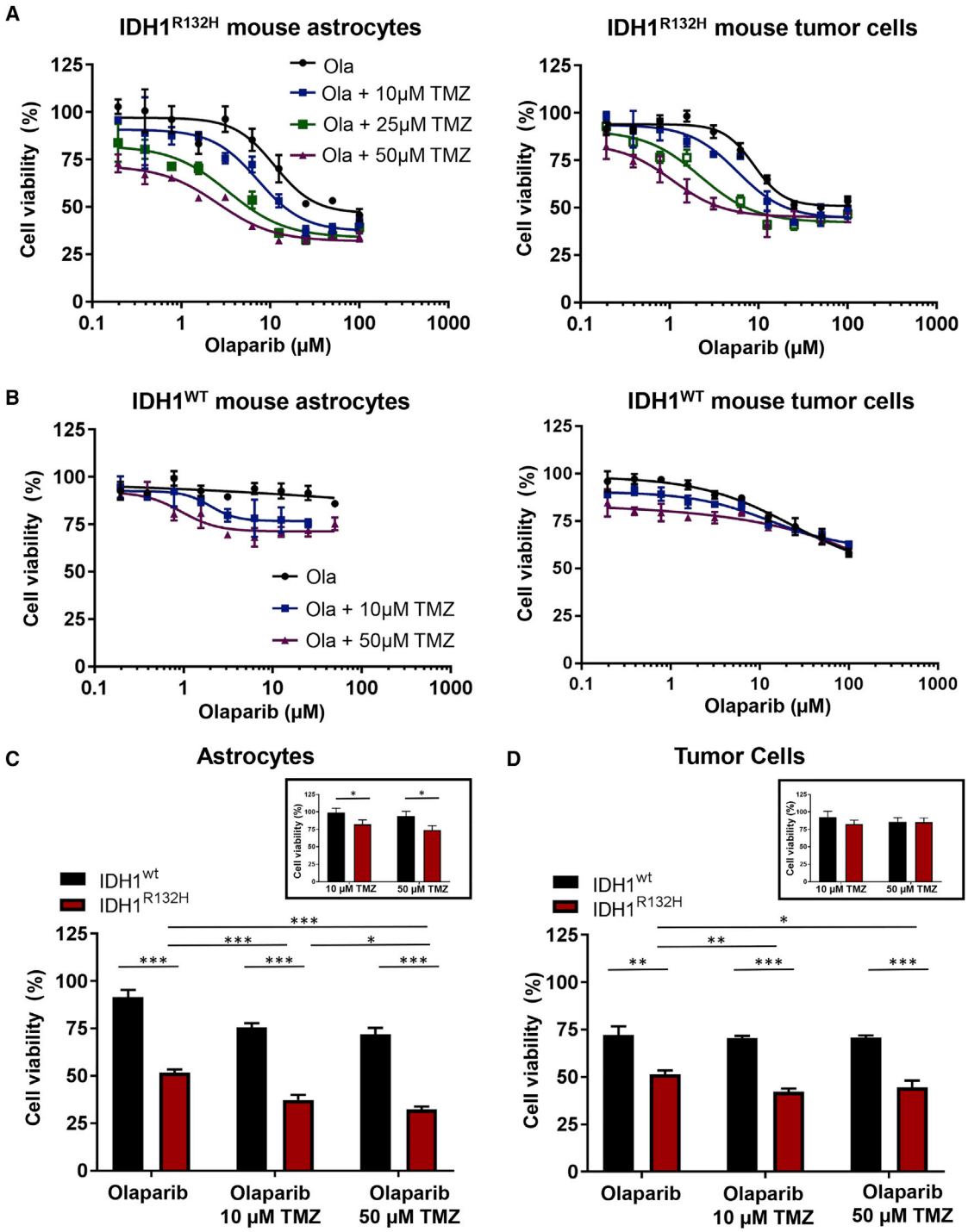

Figure 7. Astrocytes and Glioma Cells Harboring IDH1^{R132H} Demonstrate Enhanced Sensitivity to Inhibition of PARP-Mediated DNA Repair and Potentiation by Alkylating Chemotherapy

(A) Dose-response curves for N::*TVA*;*Cdkn2a*$^{lox/lox}$;*Atrx*$^{lox/lox}$;*Pten*$^{lox/lox}$ mouse astrocytes (left panel) and tumor cells (right panel) expressing PDGFA, Cre, and IDH1^{R132H} treated with olaparib and TMZ.

(B) Dose-response curves for N::*TVA*;*Cdkn2a*$^{lox/lox}$;*Atrx*$^{lox/lox}$;*Pten*$^{lox/lox}$ mouse astrocytes and tumor cells expressing PDGFA, Cre, and WT IDH1 treated with olaparib and TMZ.

(legend continued on next page)

Utah. Both male and female newborn through adult mice were used in this study.

DATA AND SOFTWARE AVAILABILITY

The accession number for RNA sequencing (RNA-seq) and methylation array data reported in this paper is GEO: GSE107616.

SUPPLEMENTAL INFORMATION

Supplemental Information includes Supplemental Experimental Procedures, five figures, and two tables and can be found with this article online at https://doi.org/10.1016/j.celrep.2018.03.133.

ACKNOWLEDGMENTS

We thank the members of the Koh, VanBrocklin, and Holmen labs as well as E. Holland, R. DePinho, and M. Bosenberg for providing mouse strains, reagents, and advice. We thank the Huntsman Cancer Institute (HCI) Vivarium staff for assistance with mouse husbandry. We thank Tim Parnell for bioinformatics expertise and Rowan Arave for assistance with the graphical abstract. We acknowledge the use of the Mass Spectrometry Core, the DNA Synthesis Core, the DNA Sequencing Core, the Small Animal Imaging Core, and the Drug Discovery Core at the University of Utah. We also acknowledge use of the HCI Shared Resources for High-Throughput Genomics and Bioinformatics analysis and the Biorepository Molecular Pathology (BMP) Research Histology Section supported by P30CA042014 awarded to HCI from the National Cancer Institute (NCI). This work was supported by the National Institute of Neurological Disorders and Stroke (R01NS075155) and NCI (F30CA203096).

AUTHOR CONTRIBUTIONS

B.P., D.X.Y., M.R.S., C.H.S., J.P.R., H.C., G.L.R., M.W.V., and S.L.H. contributed to the experimental design. B.P. performed the majority of the experiments. S.N.A. was responsible for breeding and genotyping. A.E.W. and S.R.T. performed immunohistochemistry. J.A.S. provided pathological analysis. R.J.G. created the *Atrx-floxed* mice. R.E.L. prepared the TFMB-(R)-2HG. B.P., D.X.Y., M.R.S., and S.L.H. prepared the manuscript.

DECLARATION OF INTERESTS

The authors declare no competing interests.

Received: January 3, 2018
Revised: February 23, 2018
Accepted: March 29, 2018
Published: May 1, 2018

REFERENCES

Almeida, J.S., Iriabho, E.E., Gorrepati, V.L., Wilkinson, S.R., Grüneberg, A., Robbins, D.E., and Hackney, J.R. (2012). ImageJS: Personalized, participated, pervasive, and reproducible image bioinformatics in the web browser. J. Pathol. Inform. *3*, 25.

Amankulor, N.M., Kim, Y., Arora, S., Kargl, J., Szulzewsky, F., Hanke, M., Margineantu, D.H., Rao, A., Bolouri, H., Delrow, J., et al. (2017). Mutant IDH1 regulates the tumor-associated immune system in gliomas. Genes Dev. *31*, 774–786.

Bardella, C., Al-Dalahmah, O., Krell, D., Brazauskas, P., Al-Qahtani, K., Tomkova, M., Adam, J., Serres, S., Lockstone, H., Freeman-Mills, L., et al. (2016). Expression of Idh1^{R132H}in the murine subventricular zone stem cell niche recapitulates features of early gliomagenesis. Cancer Cell *30*, 578–594.

Boehmer, C., Okur, F., Setiawan, I., Bröer, S., and Lang, F. (2003). Properties and regulation of glutamine transporter SN1 by protein kinases SGK and PKB. Biochem. Biophys. Res. Commun. *306*, 156–162.

Brat, D.J., Verhaak, R.G., Aldape, K.D., Yung, W.K., Salama, S.R., Cooper, L.A., Rheinbay, E., Miller, C.R., Vitucci, M., Morozova, O., et al.; Cancer Genome Atlas Research Network (2015). Comprehensive, integrative genomic analysis of diffuse lower-grade gliomas. N. Engl. J. Med. *372*, 2481–2498.

Cairncross, J.G., Wang, M., Jenkins, R.B., Shaw, E.G., Giannini, C., Brachman, D.G., Buckner, J.C., Fink, K.L., Souhami, L., Laperriere, N.J., et al. (2014). Benefit from procarbazine, lomustine, and vincristine in oligodendroglial tumors is associated with mutation of IDH. J. Clin. Oncol. *32*, 783–790.

Cimino, P.J., Zager, M., McFerrin, L., Wirsching, H.G., Bolouri, H., Hentschel, B., von Deimling, A., Jones, D., Reifenberger, G., Weller, M., and Holland, E.C. (2017). Multidimensional scaling of diffuse gliomas: Application to the 2016 World Health Organization classification system with prognostically relevant molecular subtype discovery. Acta Neuropathol. Commun. *5*, 39.

Cohen, A.L., Holmen, S.L., and Colman, H. (2013). IDH1 and IDH2 mutations in gliomas. Curr. Neurol. Neurosci. Rep. *13*, 345.

Cohen, A., Sato, M., Aldape, K., Mason, C.C., Alfaro-Munoz, K., Heathcock, L., South, S.T., Abegglen, L.M., Schiffman, J.D., and Colman, H. (2015). DNA copy number analysis of Grade II-III and Grade IV gliomas reveals differences in molecular ontogeny including chromothripsis associated with IDH mutation status. Acta Neuropathol. Commun. *3*, 34.

Dang, L., White, D.W., Gross, S., Bennett, B.D., Bittinger, M.A., Driggers, E.M., Fantin, V.R., Jang, H.G., Jin, S., Keenan, M.C., et al. (2009). Cancer-associated IDH1 mutations produce 2-hydroxyglutarate. Nature *462*, 739–744.

Dang, L., Yen, K., and Attar, E.C. (2016). IDH mutations in cancer and progress toward development of targeted therapeutics. Ann. Oncol. *27*, 599–608.

Draskovic, I., Arnoult, N., Steiner, V., Bacchetti, S., Lomonte, P., and Londoño-Vallejo, A. (2009). Probing PML body function in ALT cells reveals spatiotemporal requirements for telomere recombination. Proc. Natl. Acad. Sci. USA *106*, 15726–15731.

Flavahan, W.A., Drier, Y., Liau, B.B., Gillespie, S.M., Venteicher, A.S., Stemmer-Rachamimov, A.O., Suvà, M.L., and Bernstein, B.E. (2016). Insulator dysfunction and oncogene activation in IDH mutant gliomas. Nature *529*, 110–114.

Garrick, D., Sharpe, J.A., Arkell, R., Dobbie, L., Smith, A.J., Wood, W.G., Higgs, D.R., and Gibbons, R.J. (2006). Loss of Atrx affects trophoblast development and the pattern of X-inactivation in extraembryonic tissues. PLoS Genet. *2*, e58.

Holland, E.C. (2000). A mouse model for glioma: Biology, pathology, and therapeutic opportunities. Toxicol. Pathol. *28*, 171–177.

Hu, Y., Shi, G., Zhang, L., Li, F., Jiang, Y., Jiang, S., Ma, W., Zhao, Y., Songyang, Z., and Huang, J. (2016). Switch telomerase to ALT mechanism by inducing telomeric DNA damages and dysfunction of ATRX and DAXX. Sci. Rep. *6*, 32280.

Jiang, W.-Q., Zhong, Z.-H., Nguyen, A., Henson, J.D., Toouli, C.D., Braithwaite, A.W., and Reddel, R.R. (2009). Induction of alternative

(C) Quantification of cell viability in mouse astrocytes expressing wild-type or mutant IDH1 treated with olaparib alone (25 μM), TMZ alone (10 μM, 50 μM; inset), and olaparib in combination with TMZ.
(D) Quantification of cell viability in wild-type and mutant IDH1 glioma-derived cells treated with olaparib alone (25 μM), TMZ alone (10 μM, 50 μM; inset), and in combination with TMZ.
Data are expressed as the mean ± SEM with three replicates. Significance is denoted: *$p < 0.05$, **$p < 0.01$, ***$p < 0.001$.

lengthening of telomeres-associated PML bodies by p53/p21 requires HP1 proteins. J. Cell Biol. *185*, 797–810.

Lenting, K., Verhaak, R., Ter Laan, M., Wesseling, P., and Leenders, W. (2017). Glioma: Experimental models and reality. Acta Neuropathol. *133*, 263–282.

Losman, J.A., Looper, R.E., Koivunen, P., Lee, S., Schneider, R.K., McMahon, C., Cowley, G.S., Root, D.E., Ebert, B.L., and Kaelin, W.G., Jr. (2013). (R)-2-hydroxyglutarate is sufficient to promote leukemogenesis and its effects are reversible. Science *339*, 1621–1625.

Lu, F., Chen, Y., Zhao, C., Wang, H., He, D., Xu, L., Wang, J., He, X., Deng, Y., Lu, E.E., et al. (2016). Olig2-dependent reciprocal shift in PDGF and EGF receptor signaling regulates tumor phenotype and mitotic growth in malignant glioma. Cancer Cell *29*, 669–683.

Lu, Y., Kwintkiewicz, J., Liu, Y., Tech, K., Frady, L.N., Su, Y.T., Bautista, W., Moon, S.I., MacDonald, J., Ewend, M.G., et al. (2017). Chemosensitivity of IDH1-mutated gliomas due to an impairment in PARP1-mediated DNA repair. Cancer Res. *77*, 1709–1718.

Modrek, A.S., Golub, D., Khan, T., Bready, D., Prado, J., Bowman, C., Deng, J., Zhang, G., Rocha, P.P., Raviram, R., et al. (2017). Low-grade astrocytoma mutations in IDH1, P53, and ATRX cooperate to block differentiation of human neural stem cells via repression of SOX2. Cell Rep. *21*, 1267–1280.

Mukherjee, J., Johannessen, T.A., Ohba, S., Chow, T.T., Jones, L.E., Pandita, A., and Pieper, R.O. (2018). Mutant IDH1 co-operates with ATRX loss to drive the alternative lengthening of telomere (ALT) phenotype in glioma. Cancer Res. Published online March 15, 2018. https://doi.org/10.1158/0008-5472.CAN-17-2269.

Noushmehr, H., Weisenberger, D.J., Diefes, K., Phillips, H.S., Pujara, K., Berman, B.P., Pan, F., Pelloski, C.E., Sulman, E.P., Bhat, K.P., et al.; Cancer Genome Atlas Research Network (2010). Identification of a CpG island methylator phenotype that defines a distinct subgroup of glioma. Cancer Cell *17*, 510–522.

Ozawa, T., Riester, M., Cheng, Y.K., Huse, J.T., Squatrito, M., Helmy, K., Charles, N., Michor, F., and Holland, E.C. (2014). Most human non-GCIMP glioblastoma subtypes evolve from a common proneural-like precursor glioma. Cancer Cell *26*, 288–300.

Parsons, D.W., Jones, S., Zhang, X., Lin, J.C., Leary, R.J., Angenendt, P., Mankoo, P., Carter, H., Siu, I.M., Gallia, G.L., et al. (2008). An integrated genomic analysis of human glioblastoma multiforme. Science *321*, 1807–1812.

Pietrak, B., Zhao, H., Qi, H., Quinn, C., Gao, E., Boyer, J.G., Concha, N., Brown, K., Duraiswami, C., Wooster, R., et al. (2011). A tale of two subunits: How the neomorphic R132H IDH1 mutation enhances production of αHG. Biochemistry *50*, 4804–4812.

Robinson, J.P., VanBrocklin, M.W., Guilbeault, A.R., Signorelli, D.L., Brandner, S., and Holmen, S.L. (2010). Activated BRAF induces gliomas in mice when combined with Ink4a/Arf loss or Akt activation. Oncogene *29*, 335–344.

Rohle, D., Popovici-Muller, J., Palaskas, N., Turcan, S., Grommes, C., Campos, C., Tsoi, J., Clark, O., Oldrini, B., Komisopoulou, E., et al. (2013). An inhibitor of mutant IDH1 delays growth and promotes differentiation of glioma cells. Science *340*, 626–630.

Sanson, M., Marie, Y., Paris, S., Idbaih, A., Laffaire, J., Ducray, F., El Hallani, S., Boisselier, B., Mokhtari, K., Hoang-Xuan, K., and Delattre, J.Y. (2009). Isocitrate dehydrogenase 1 codon 132 mutation is an important prognostic biomarker in gliomas. J. Clin. Oncol. *27*, 4150–4154.

Sasaki, M., Knobbe, C.B., Itsumi, M., Elia, A.J., Harris, I.S., Chio, I.I., Cairns, R.A., McCracken, S., Wakeham, A., Haight, J., et al. (2012). D-2-hydroxyglutarate produced by mutant IDH1 perturbs collagen maturation and basement membrane function. Genes Dev. *26*, 2038–2049.

Shin, C.H., Robinson, J.P., Sonnen, J.A., Welker, A.E., Yu, D.X., VanBrocklin, M.W., and Holmen, S.L. (2017). HBEGF promotes gliomagenesis in the context of Ink4a/Arf and Pten loss. Oncogene *36*, 4610–4618.

Sulkowski, P.L., Corso, C.D., Robinson, N.D., Scanlon, S.E., Purshouse, K.R., Bai, H., Liu, Y., Sundaram, R.K., Hegan, D.C., Fons, N.R., et al. (2017). 2-Hydroxyglutarate produced by neomorphic IDH mutations suppresses homologous recombination and induces PARP inhibitor sensitivity. Sci. Transl. Med. *9*, Published online February 1, 2017. https://doi.org/10.1126/scitranslmed.aal2463.

Tahiliani, M., Koh, K.P., Shen, Y., Pastor, W.A., Bandukwala, H., Brudno, Y., Agarwal, S., Iyer, L.M., Liu, D.R., Aravind, L., and Rao, A. (2009). Conversion of 5-methylcytosine to 5-hydroxymethylcytosine in mammalian DNA by MLL partner TET1. Science *324*, 930–935.

Tran, A.N., Lai, A., Li, S., Pope, W.B., Teixeira, S., Harris, R.J., Woodworth, D.C., Nghiemphu, P.L., Cloughesy, T.F., and Ellingson, B.M. (2014). Increased sensitivity to radiochemotherapy in IDH1 mutant glioblastoma as demonstrated by serial quantitative MR volumetry. Neuro-oncol. *16*, 414–420.

Verhaak, R.G., Hoadley, K.A., Purdom, E., Wang, V., Qi, Y., Wilkerson, M.D., Miller, C.R., Ding, L., Golub, T., Mesirov, J.P., et al.; Cancer Genome Atlas Research Network (2010). Integrated genomic analysis identifies clinically relevant subtypes of glioblastoma characterized by abnormalities in PDGFRA, IDH1, EGFR, and NF1. Cancer Cell *17*, 98–110.

Weller, M., Felsberg, J., Hartmann, C., Berger, H., Steinbach, J.P., Schramm, J., Westphal, M., Schackert, G., Simon, M., Tonn, J.C., et al. (2009). Molecular predictors of progression-free and overall survival in patients with newly diagnosed glioblastoma: A prospective translational study of the German Glioma Network. J. Clin. Oncol. *27*, 5743–5750.

Xu, X., Zhao, J., Xu, Z., Peng, B., Huang, Q., Arnold, E., and Ding, J. (2004). Structures of human cytosolic NADP-dependent isocitrate dehydrogenase reveal a novel self-regulatory mechanism of activity. J. Biol. Chem. *279*, 33946–33957.

Xu, W., Yang, H., Liu, Y., Yang, Y., Wang, P., Kim, S.H., Ito, S., Yang, C., Wang, P., Xiao, M.T., et al. (2011). Oncometabolite 2-hydroxyglutarate is a competitive inhibitor of α-ketoglutarate-dependent dioxygenases. Cancer Cell *19*, 17–30.

Yan, H., Bigner, D.D., Velculescu, V., and Parsons, D.W. (2009a). Mutant metabolic enzymes are at the origin of gliomas. Cancer Res. *69*, 9157–9159.

Yan, H., Parsons, D.W., Jin, G., McLendon, R., Rasheed, B.A., Yuan, W., Kos, I., Batinic-Haberle, I., Jones, S., Riggins, G.J., et al. (2009b). IDH1 and IDH2 mutations in gliomas. N. Engl. J. Med. *360*, 765–773.

Zdzisińska, B., Żurek, A., and Kandefer-Szerszeń, M. (2017). Alpha-ketoglutarate as a molecule with pleiotropic activity: Well-known and novel possibilities of therapeutic use. Arch. Immunol. Ther. Exp. (Warsz.) *65*, 21–36.

Zheng, H., Ying, H., Yan, H., Kimmelman, A.C., Hiller, D.J., Chen, A.J., Perry, S.R., Tonon, G., Chu, G.C., Ding, Z., et al. (2008). p53 and Pten control neural and glioma stem/progenitor cell renewal and differentiation. Nature *455*, 1129–1133.

Cell Reports, Volume *23*

Supplemental Information

Mutant *IDH1* Promotes Glioma Formation *In Vivo*

Beatrice Philip, Diana X. Yu, Mark R. Silvis, Clifford H. Shin, James P. Robinson, Gemma L. Robinson, Adam E. Welker, Stephanie N. Angel, Sheryl R. Tripp, Joshua A. Sonnen, Matthew W. VanBrocklin, Richard J. Gibbons, Ryan E. Looper, Howard Colman, and Sheri L. Holmen

Supplemental Experimental Procedures

Genotyping

Genotyping for the TVA transgene was carried out in 25 μL total volume containing 2.5 μL 10X PCR buffer (Life Technologies), 10 μL DMSO, 125 μL 50 mmol/l $MgCl_2$, 0.625 mmol/l of each nucleotide, 1 unit of Taq polymerase (Life Technologies), 6.25 μg/ml of primers TVA-386 sense and TVA-786 antisense to detect a 400-bp fragment. Samples were amplified for 30 cycles (94 °C for 30 seconds, 56 °C for 30 seconds, and 72 °C for 45 seconds) (Shin et al., 2017). PCR to detect a 180-bp *Cdkn2a*$^{lox/lox}$ allele and a 140-bp wild-type *Cdkn2a* allele was carried out with specific primers. Cycling conditions are 94 ˚C for 1 min followed by 30 cycles of 94 ˚C for 30 s, annealing for 30 s at 55 ˚C, elongation for 30 s and a final extension at 72 ˚C for 7 minutes (Shin et al., 2017). Genotyping for *Pten*^{lox}, and wild-type alleles was performed to detect 1000-bp *Pten*^{lox} allele and an 811-bp *Pten* wild type allele using CFP1, R1NEOCP and PTR14 primers. Cycling conditions are 95 ˚C for 3 min followed by 28 cycles of 95 ˚C for 1 min, annealing for 1 min at 60 ˚C and elongation at 72 ˚C for 1 min and a final extension at 72 ˚C for 6 min (Shin et al., 2017). PCR to detect a 2500-bp *Atrx*^{lox} allele and a 2000-bp wild-type *Atrx* allele was carried out using AccuStart II PCR SuperMix (Quantabio) per the manufacturer's specifications. Cycling conditions were as follows: 94 ˚C for 2 min followed by 34 cycles of 94 ˚C for 15 s, annealing for 30 s at 55 ˚C and elongation at 72 ˚C for 3 minutes.

Viral constructs and propagation

The avian retroviral vectors used in this study are replication-competent Avian Leukosis Virus (ALV) with Bryan polymerase subgroup A (designated RCASBP(A) and abbreviated RCAS). RCAS-*X* was a gift from Harold Varmus. RCAS-*Cre* has been described previously (Robinson et al., 2010). RCAS-*PDGFA* was cloned using LR recombination from the Gateway PLUS shuttle X03795.1 (Genecopoeia). *IDH1* (ENST00000345146.6) was PCR amplified from a cDNA library generated from normal human astrocytes (ScienCell Research Laboratories). The R132H mutation and C-terminal HA epitope tag were introduced using PCR (primer sequences are available upon request). The PCR products were cloned into the pCR8/GW/Topo vector (Thermo Fisher Scientific (TFS)), bidirectionally verified using Sanger sequencing, and Gateway cloned into the RCAS destination vector using LR Clonase II per the manufacturer's specifications (TFS). Viral infection was initiated by calcium phosphate transfection of proviral DNA into DF-1 avian fibroblasts. DF-1 cells were maintained in DMEM with 10% FBS, 100 IU/ml gentamicin, and 100 units/ml penicillin/streptomycin at 37 °C. Viral spread was monitored by expression of the p27 viral capsid protein as determined by western blot (Shin et al., 2015).

Viral delivery in vivo

Infected DF-1 cells from a confluent 10-cm culture dish were pelleted and re-suspended in 50 µl HBSS. Newborn pups were injected 2 mm ventral to Bregma with 5 µl of cell suspension using a gas-tight Hamilton syringe. In order to directly compare all of the different groups of mice in our study, three viruses were delivered to each mouse to maintain equal amounts of virus for each cohort. In groups with fewer than three delivered genes, an empty vector (RCAS-X) was co-injected to effectively dilute viral ratios to those equal to what would be expected for injections with three RCAS viruses.

Histological analysis

Brain tissue from injected mice was isolated, fixed in neutral buffered formalin (NBF), and paraffin embedded. 5 µm sections from tissue blocks were adhered to glass slides and stained by H&E or left unstained for further analysis.

Immunohistochemistry (IHC)

Tissue sections were deparaffinized as previously described (Vanbrocklin et al., 2012). IHC was performed with the following antibodies: HA (1/250), OLIG2 (1/300), ATRX (1/250), GFAP (1/200) PTEN (1/150), p19ARF (1/250), Ki67 (1/100), Endomucin (1/300) and $IDH1^{R132H}$ (1/30), 5hmc (1/2500), and PDGFA (1/250). Specific details regarding the staining procedures are available upon request. Slides were imaged on a Zeiss Axio microscope equipped with a 5 megapixel camera.

Development of primary astrocyte cell lines

N*::TVA*;$Cdkn2a^{lox/lox}$ astrocytes have been described (Robinson et al., 2010). N*::TVA*;$Atrx^{lox/lox}$; N*::TVA*;$Cdkn2a^{lox/lox}$;$Atrx^{lox/lox}$; and N*::TVA*;$Cdkn2a^{lox/lox}$;$Atrx^{lox/lox}$;$Pten^{lox/lox}$ primary astrocytes were established following dissection of newborn mouse brain tissue by physical disruption into single cells using scalpels and 0.25% trypsin. Cell cultures were maintained in DMEM (Invitrogen) containing 10% FBS, 100 IU/ml gentamicin, and 100 units/ml penicillin/streptomycin.

Viral infections in vitro

Astrocytes from newborn mice were seeded in six-well plates at a density of 5×10^4 cells/well and were maintained in DMEM with 10% FBS, 100 IU/ml gentamicin, and 100 units/ml penicillin/streptomycin at 37 °C. Prior to infection, the media was removed and replaced with 1 ml of filtered virus-containing media with 8 mg/ml polybrene

(Sigma) and incubated overnight at 37 °C. Infected astrocyte cultures were maintained as described above except the culture media was supplemented with 2 mM glutamine.

Immunoblotting

Whole cell lysates were collected using SDS-lysis buffer (200 mM Tris/HCl pH 6.8), 2% SDS, 0.1 M DTT, 10% Glycerol, 0.1% bromophenol Blue) or RIPA buffer with the addition of protease inhibitor cocktail (Bio-Rad Laboratories). Proteins were separated on 8-16% Tris-glycine polyacrylamide gels or 6% polyacrylamide gels (Invitrogen) for proteins above 200 KDa and transferred to nitrocellulose or PVDF membranes. Blots were probed with the indicated primary and secondary antibodies, incubated with Amersham ECL Western Blotting Detection Reagents (GE Healthcare), and exposed to film. Primary antibodies used were: Rabbit anti-IDH1 (1:1000); Mouse anti-IDH^{R132H} (1:1000) Mouse anti-GAPDH (1:1000); Rabbit anti-HA (1:1000); Rabbit polyclonal PDGFA (1:1000); Rabbit polyclonal ATRX (1:1000) Rabbit anti-PTEN (1:1000); p19ARF (1:1000). HRP-conjugated secondary antibodies used were: anti-Mouse IgG (1:1000) and anti-Rabbit IgG (1:1000). The source of the antibodies used is indicated in the Resource Table.

Synthesis of TFMB–(R)-2HG

To a solution of (*R*) oxotetrahydrofuran-2-carboxylic acid (650 mg, 5.0 mmol) in acetonitrile (15 ml) was added *i*-Pr2NEt (1.05 ml, 6.0 mmol, 1.2 equiv) and 3-(trifluoromethyl) benzyl bromide (0.92 ml, 6.0 mmol, 1.2 equiv). The mixture was heated to reflux for 10 minutes and allowed to stir at RT overnight. The mixture was concentrated under reduced pressure and the resulting residue taken up in ethyl acetate (50 ml). The organics were washed with 10% HCl (50 ml), 10% sat $NaHCO_3$ (50 ml) and brine (50 ml) and were dried over Na_2SO_4. Concentration gave a light yellow oil which was purified on silica gel, eluting with 1:1 hexanes:ethyl acetate to give the title compounds [(*R*)-enantiomer: 1.28 g, 89%] as a clear oil which later solidified upon standing in the freezer. Physical characteristics are detailed in (Losman et al., 2013).

Proliferation assay

Cell proliferation was assessed using an MTT (3-(4,5-Dimethylthiazol-2-yl)-2,5-Diphenyltetrazolium Bromide) (Life technologies) assay. Briefly, 1×10^3 cells were seeded into each well of a 96 well plate. MTT, 20 µl (final concentration 1 mg/ml), was added to the cells at 24, 48, and 72 h post culture and incubated for 4 h at 37 °C. For proliferation assays using 2-HG, the media was supplemented with 3 mM TFMB–(R)-2HG. Excess MTT reagent

was removed and the formazan crystals were dissolved in 100 µl of DMSO and quantified via absorbance at 570 nm.

Soft agar colony formation assay

To assess anchorage-independent growth, 1.5×10^5 cells were suspended in 0.35% Difco Noble Agar (Becton Dickinson) in DMEM with 10% FBS and layered onto 0.65% pre-solidified Difco Noble Agar in DMEM with 10% FBS. Culture media with or without 3mM TFMB–(R)-2HG was replenished every 3 days for 3 weeks.

2-HG Analysis

Two 10 cm plates of N*::TVA;Cdkn2a*$^{lox/lox}$*;Atrx*$^{lox/lox}$*;Pten*$^{lox/lox}$ primary astrocytes infected with viruses containing the genes indicated were pelleted and snap frozen at -80 °C. For mass spectrometry analysis of 2-HG, cells were suspended in 90% methanol containing d_4-succinate. Absolute concentrations of R-2-HG in samples were determined from a calibration curve. Samples were extracted in 1 ml 90% ice cold MeOH, then spiked with the internal standard (10 ng of d3-2-HG), sonicated for 2 min and then incubated at -20 °C for 1 hr. Samples were then centrifuged at 4 °C for 10 min at 15,000 G. The supernatants were dried overnight in a speedVac. Samples were derivatized by the addition of 160 µl N -(p-toluenesulfonyl-L-phenylalanyl chloride (TSPC)) [1.25 mM in anhydrous acetonitrile (ACN)] and 2 µl of pyridine followed by 10 min incubation at room temperature, desiccated, resuspended in 100 µl ACN/H_2O (1:1) and transferred to a glass LC/MS vial for analysis. All experiments were performed using an Agilent 1290 Infinity UHPLC system and an Agilent 6490 triple quadrupole (QqQ) mass spectrometer interfaced with an Electron spray ionization (ESI) source. Separations were achieved using a RP column (Phenomenex Luna 5 µm C18 (2) 250 × 2.1 mm) operated at room temperature, while the autosampler was set at 4 °C. Injection volume was 3 µl. The chromatography gradient is isocratic for 18 min consisting of 38% mobile phase A (0.1% FA in water) and 62% mobile phase B (1:1 ACN:MeOH), then brought to 99% mobile phase B at 19 min and held for 6 min, and then returned to initial conditions and equilibrated for 8 min using a flow rate of 0.5 ml/min. The Agilent 6490 triple quadrupole mass was operated in the negative ion mode. The mass transitions (precursor → product ions) were 448.1 → 317.9 and 448.1 → 154.8 for TSPC-2HG, and 451.1 → 317.9 and 451.1 → 154.8 for internal standard d3-TSPC-2HG. The MRM acquisition parameters used were as follows: 4000 V capillary voltage, 500 V nozzle voltage, 12 l/min sheath gas flow at a temperature of 350 °C (ultra-high purity nitrogen), 11 l/min drying gas flow at a temperature of 150 °C, 35 psi nebulizer gas flow, 380 V default fragmentor voltage, 4 V or 1 V transition-specific cell accelerator potential, 9 - 41 V transitions-specific collision energy (CE),

and unit resolution. The MRM parameters were optimized to achieve maximum sensitivity. Results from LC-MS experiments were collected using Agilent Mass Hunter Workstation B.07.01 and analyzed using the software packages Mass Hunter Quant B.07.00 and Microsoft Excel.

NADPH assay

IDH1 activity was measured using an Isocitrate Dehydrogenase Activity Colorimetric Assay Kit (BioVision) per the manufacturer's protocol. Briefly, 1×10^6 cells were washed in ice cold PBS and homogenized in 200 µl IDH assay buffer. Five µg of protein extracted from each sample was transferred to a 96-well plate and mixed with the assay reaction mix in 1:1 ratio in triplicate. The plate was incubated at 37 °C and OD 450 was recorded every 5 min for 2 h using the Synergy HT Multi-Detection Microplate Reader (Bio-Tek). NADPH values were calculated from standard curves.

Immuno-Fluorescent In Situ Hybridization (Immuno-FISH)

To detect the ALT phenotype in tumor tissue, we performed Immuno-FISH. Briefly, 5 µm sections were de-paraffinized and subjected to heat induced antigen retrieval. Slides were washed with PBS, incubated in 0.005% pepsin solution for 5 min at 37 °C, followed by 2 washes in PBS and dehydration in ice cold ethanol. 200 nM of Alexa Fluor 488 conjugated C rich telomere probe (PNA Bio) prepared in 20 µl hybridization buffer (Roche Diagnostics) was applied to the slides and incubated for 10 min at 85 °C followed by 2 h incubation in the dark to allow hybridization. Post hybridization, the slides were incubated with PML antibody for 1 h followed by incubation with Alexa Flour 594 conjugated donkey anti-mouse secondary antibody. Cell nuclei were counterstained with Hoechst 33342 (Life Technologies) and mounted with ProLong Gold Antifade reagent (Life Technologies). Slides were imaged using a 100X oil immersion objective on a Zeiss Axioskop 2 MOT Plus fluorescence microscope.

Bioinformatics and Genomics

For RNAseq analysis, mouse tumors were microdissected from 10 µm FFPE sections and extracted using the Ambion Recoverall Kit (Ambion). Samples were prepped with TruSeq Stranded Total RNA with Ribo-Zero Gold and then sequenced on HiSeq 50 Cycle Single-Read Sequencing v4 (Illumina). Reads were aligned to the mouse genome (mm10) and differential gene expression was determined with the open source USeq/DESeq2 package. Genes were selected using two thresholds, an FDR of <10% and absolute log2 ratio > 1. GBM classifier genes were accessed from the TCGA data portal and were converted to mouse orthologues genes using Biomart (Verhaak et al., 2010). GSEA (v2. 2.0) was used to analyze the enrichment of signature gene sets from different GBM subtypes as

described (Lu et al., 2016). For Methylation array, Bisulfite sequencing library was prepared using an Agilent SureSelect XT Mouse Methyl-Seq capture kit following manufacturer's recommendations. The library was sequenced on an Illumina HiSeq 2500 multiplexed with 4 samples per lane. Reads were de-multiplexed and converted to Fastq using Illumina's pipeline. Reads were aligned to the mouse genome (build mm10, UCSC) using Novocraft Novoalign (www.novocraft.com, version 3.7.1) in bisulfite mode using options -b 2 -t 360 -h 120 -r random. Duplicate alignments were removed using Picard MarkDuplicates (http://broadinstitute.github.io/picard/index.html, version 2.9.0). Bisulfite analysis was performed with the USeq application (https://github.com/HuntsmanCancerInstitute/USeq/tree/master/Source, version 9.0.8). Cytosine methylation observations were converted to point data using USeq NovoalignBisulfiteParser, increasing minimum base quality to 20 and minimum map quality to 13. Point data was filtered for CpG contexts using USeq ParsePointDataContexts. For regional differential methylation analysis, USeq DefinedRegionBisSeq was run with a minimum base read coverage of 10. There were 220,894 target regions tested, representing intervals with a minimum mean base coverage of 10 reads across all samples and a minimum length of 100-bp. They were identified using Macs2 bdgpeakcall with a bedgraph representation of average read depth across all samples. Differentially methylated regions were filtered using criteria of absolute pseudomedian log2 ratio difference >= 1.0 and a -10log10 transformed Benjamini & Hochberg corrected FDR>30. To generate the regional methylation score, USeq ScoreMethylatedRegions was run with a minimum read coverage of 10 over the filtered targets; targets without a score across all samples were removed. Heat maps and figures were generated in R using the collected region sum fraction methylation score. Differentially methylated targets were annotated with the R package Chipseeker.

Cell viability assays

High-throughput *in vitro* cell viability assays were performed at the University of Utah Drug Discovery Core facility. Briefly, the activity levels of TMZ and olaparib as single agents in mouse astrocytes was determined by high-throughput CellTiter-Glo cell viability assay (Promega). Cells (1×10^3) were plated in each well of 384–well plates using the Tecan EVO100/MCA384 liquid handling station in a sterile bio-hood and incubated overnight. Drugs were added to the wells 24 hours after cell plating using the Tecan D300e Digital Dispenser, which allows for picoliter to microliter non-contact dispensing of small molecules directly into the assay plate without the need for serial dilutions. Each drug concentration was applied to 4 replicate wells with four additional control wells receiving vehicle only. After 72 hours of drug incubation, CellTiter-Glo reagent was added to each well at 1:1 ratio (v/v) with

the media using the BioTek Microplate Dispenser and incubated for 30 min at room temperature. Luminescence was measured on the Synergy 4 Microplate Reader. Percent viability was calculated and used to determine IC50 values.

Resource Table

REAGENT or RESOURCE	SOURCE	IDENTIFIER
Antibodies		
Mouse anti-IDH1^{R132H}	HistoBioTec	Cat#DIA-H09
Mouse anti-PTEN (6H2.1)	Dako	Cat#M3627
Mouse anti-PML	Millipore	Cat#MAB3738
Mouse anti-GAPDH	Millipore	Cat#MAB374
Mouse anti-5hmC	Active Motif	Cat#39769
Rabbit anti-HA	Cell Signaling	Cat# 3724
Rabbit anti-Olig 2	Millipore	Cat#Ab9610
Rabbit anti-ATRX (H-300)	Santa Cruz	Cat#SC-15408
Rabbit anti-CDKN2A/p19ARF	Abcam	Cat#ab80
Rabbit anti-IDH1 (D2H1)	Cell Signaling	Cat#8137
Rabbit anti-PTEN (D4.3)	Cell Signaling	Cat#9188
Rabbit anti-PDGFA (N30)	Santa Cruz	Cat#SC-128
Rabbit anti-p19ARF	Thermo Fisher	Cat#PA1-30670
Rat anti-GFAP mAb (2.2B10)	Thermo Fisher	Cat#130300
Rat anti-Endomucin (V.7C7)	Santa Cruz	Cat#65495
Rat anti-Ki67	Dako	Cat#M7249
Anti-mouse HRP conjugated	Cell Signaling	Cat#7076s
Anti-rabbit HRP conjugated	Cell Signaling	Cat#7074
Alexa flour 594 conjugated donkey anti-mouse	Thermo Fisher	Cat#R37115
Bacterial and Virus Strains		
Escherichia coli: recA1 endA1 gyrA96 thi-1 hsdR17 supE44 relA1 lac [F´ proAB lacIq ZΔM15 Tn10 (Tetr)	Agilent Technologies	XL1-Blue Cat# 200249

Escherichia coli: F- mcrA Δ(mrr-hsdRMS-mcrBC) φ80lacZΔM15 ΔlacX74 recA1 araD139 Δ(ara- leu)7697 galU galK rpsL (StrR)	Thermo Fisher Scientific	One Shot™ TOP10 Cat# C404010
Escherichia coli: F- mcrA Δ(mrr-hsdRMS-mcrBC) Φ80lacZΔM15 ΔlacX74 recA1 araΔ139 Δ(ara-leu)7697 galU galK rpsL (StrR)	Thermo Fisher Scientific	One Shot™ *ccd*B survival™ 2 T1^{R} Cat# A10460
Escherichia coli: F- φ80(lacZ)ΔM15 ΔlacX74 hsdR(rK-mK+) ΔrecA1398 endA1 tonA	Thermo Fisher Scientific	One Shot™ Mach1™ T1 Cat# C862003
RCAS: replication-competent avian leukosis virus long terminal repeat with splice acceptor Bryan polymerase subgroup A	(Robinson et al., 2010)	NA
Biological Samples		
Mouse brain tissue	This paper	
Mouse tail biopsies	This paper	
Chemicals, Peptides, and Recombinant Proteins		
Pepsin	Sigma	Cat#P6887-1G
Hoechst 33342	Life Technologies	Cat#H3570
Prolong Gold anti-fade	Life Technologies	Cat#P10144
Temozolomide	Selleck Chemical	Cat#S1237
Olaparib	Selleck Chemical	Cat#S1060
TFMB-(*R*)-2HG	(Losman et al., 2013)	
Critical Commercial Assays		
RecoverAll™ Total Nucleic Acid Isolation Kit for FFPE	Thermo Fisher	Cat#AM1975
Ribo Zero Gold	Illumina	Cat#RS-122-2202
Isocitrate dehydrogenase kit	BioVision	Cat#K756-100
SureSelectXT Mouse Methyl-seq Reagent Kit	Agilent	Cat#931052
Qiagen DNEasy Kit	Qiagen	Cat#69504
CellTiter-Glo® Luminescent Cell Viability Assay	Promega	Cat#G7572

Deposited Data		
RNA seq processed data	This paper	https://www.ncbi.nlm.nih.gov/geo/query/acc.cgi?acc=GSE107616
Methylation array processed data	This paper	https://www.ncbi.nlm.nih.gov/geo/query/acc.cgi?acc=GSE107616
Experimental Models: Cell Lines		
N::*TVA*;*Cdkn2a*$^{lox/lox}$	(Robinson et al., 2010)	N/A
N::*TVA*;*Cdkn2a*$^{lox/lox}$;*Atrx*$^{lox/lox}$;*Pten*$^{lox/lox}$	This paper	N/A
N::*TVA*;*Cdkn2a*$^{lox/lox}$;*Atrx*$^{lox/lox}$	This paper	N/A
IDH1^{R132H} mouse tumor-derived cells	This paper	N/A
IDH1^{wt} mouse tumor-derived cells	This paper	N/A
DF-1	ATCC	Cat#CRL-12203
Experimental Models: Organisms/Strains		
N::*TVA*;*Cdkn2a*$^{lox/lox}$;*Atrx*$^{lox/lox}$;*Pten*$^{lox/lox}$	This paper	N/A
N::*TVA*;*Cdkn2a*$^{lox/lox}$;*Atrx*$^{lox/lox}$	This paper	N/A
N::*TVA*;*Cdkn2a*$^{lox/lox}$;*Pten*$^{lox/lox}$	(Shin et al., 2017)	N/A
N::*TVA*;*Atrx*$^{lox/lox}$;*Pten*$^{lox/lox}$	This paper	N/A
N::*TVA*;*Cdkn2a*$^{lox/lox}$	(Robinson et al., 2010)	N/A
N::*TVA*;*Pten*$^{lox/lox}$	(Shin et al., 2017)	N/A
N::*TVA*;*Atrx*$^{lox/lox}$	This paper	N/A
Oligonucleotides		
Primers for *TVA* 386 5′-AGCTGGTGAGATGGGACTGAAC-3′ 786 5′- CGAACATTCAAAGCCTCCAG-3′	IDT	N/A
Cdkn2a Fwd 5′-TTGTTGGCCCAGGATGCCGACATC-3′ Rev 5′-CCAAGTGTGCAAACCCAGGCTCC-3′	IDT	N/A

Primers for *Atrx* PPS1.15: 5'GGTTTTAGATGAAAATGAAGAG-3′ Mxnp30: 5'CACCATCTTCTTGCCATCTCTGTAG-3′ Neo801: 5' GGG CGC CCG GTT CTT TT-3′	IDT	N/A
Primers for *Pten* CPF1: 5'CTTCGGAGCATGTCTGGCAATGC-3′ R1NEOCP: 5'CTGCACGAGACTAGTGAGACG TGC-3′ PTR14: 5'AAGGAAGAGGGTGGGGATAC-3′	IDT	N/A
C-rich telomere probe: CCCTAACCCTAACCCTAA	PNA Bio	Cat#F1004
Recombinant DNA		
pCR8 GW TOPO HA IDH1	This paper	N/A
pCR8 GW TOPO HA IDH1 R132H	This paper	N/A
pCR8 GW TOPO PDGFA	This paper	N/A
RCAS HA IDH1	This paper	N/A
RCAS HA IDH1 R132H	This paper	N/A
RCAS HA PDGFA	This paper	N/A
RCAS X	Harold Varmus	
Software and Algorithms		
GraphPad Prism 7		*https://www.graphpad.com/scientific-software/prism/*
R statistical software Version 3.3.2		https://www.r-project.org/

Useq software version 9.0.8	(Nix et al., 2010)	https://github.com/HuntsmanCancerInstitute/USeq/tree/master/Source
Novocraft Novoalign version 3.7.1		www.novocraft.com
Image J	(Almeida et al., 2012)	http://imagejs.github.com
Mass Hunter Quant B.07.00	Agilent technologies	
Other		

Contact for Reagent and Resource Sharing

Further information and requests for resources and reagents should be directed to and will be fulfilled by the Lead Contact, Sheri L. Holmen (sheri.holmen@hci.utah.edu).

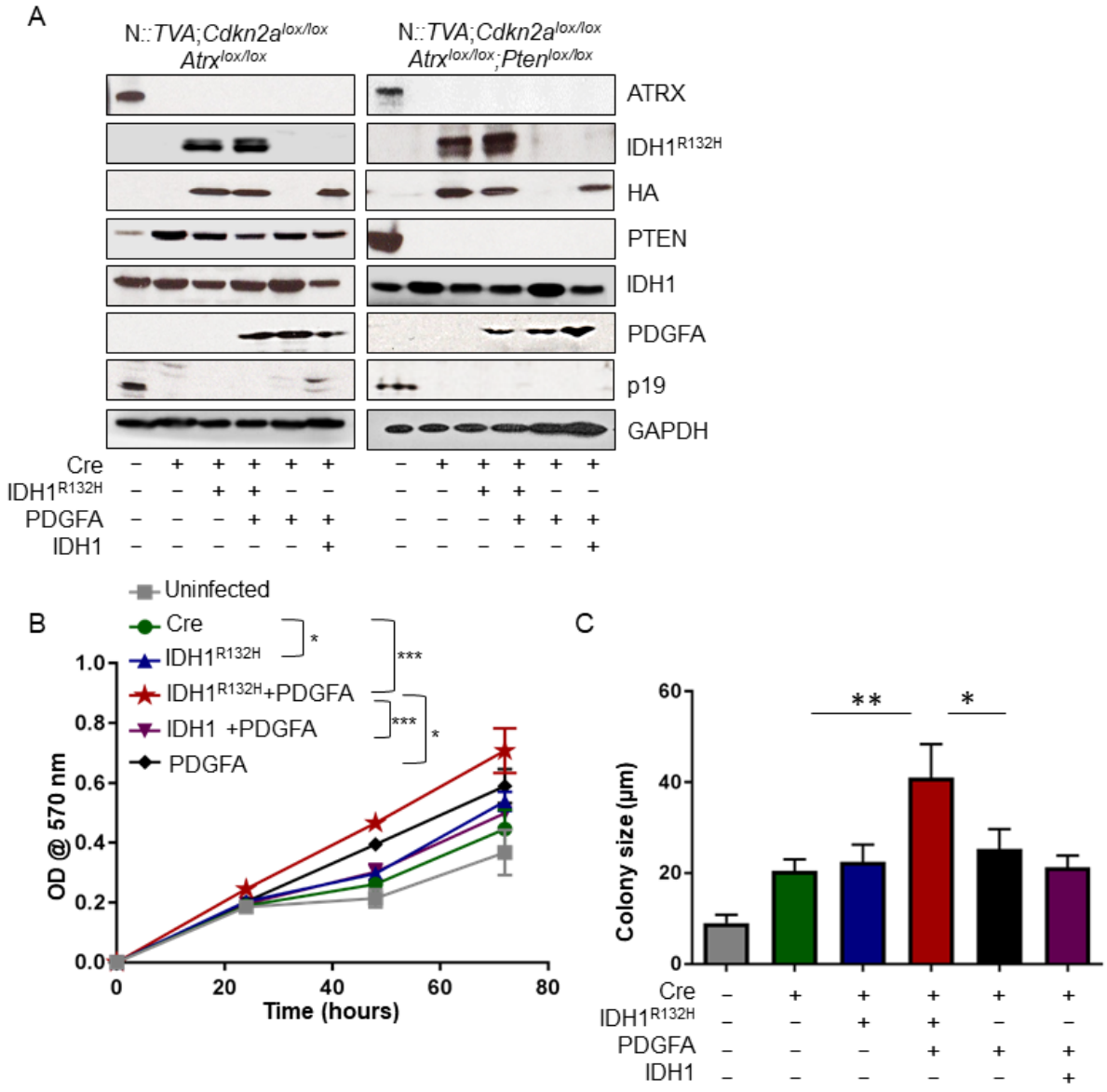

Figure S1. IDH1^{R132H} promotes proliferation and anchorage independent growth of immortal astrocytes.

Related to Figure 1. (A) Western blot analysis of ATRX, IDH1^{R132H}, HA, PTEN, IDH1, PDGFA, p19, and GAPDH in N*::TVA;Cdkn2a*$^{lox/lox}$*;Atrx*$^{lox/lox}$ (left panel) and N*::TVA;Cdkn2a*$^{lox/lox}$*;Atrx*$^{lox/lox}$*;Pten*$^{lox/lox}$ mouse astrocytes (right panel) expressing the genes indicated. (B) Analysis of cell proliferation was determined by MTT assay of astrocytes derived from N*::TVA;Cdkn2a*$^{lox/lox}$*;Atrx*$^{lox/lox}$ mice expressing the genes indicated. (C) Comparison of colony size from the soft agar colony formation assay shown in Figure 1B. Data are expressed as the mean ± S.E.M from three replicates. Statistical significance is shown by the following key: * $P < 0.05$, ** $P < 0.01$, *** $P < 0.001$.

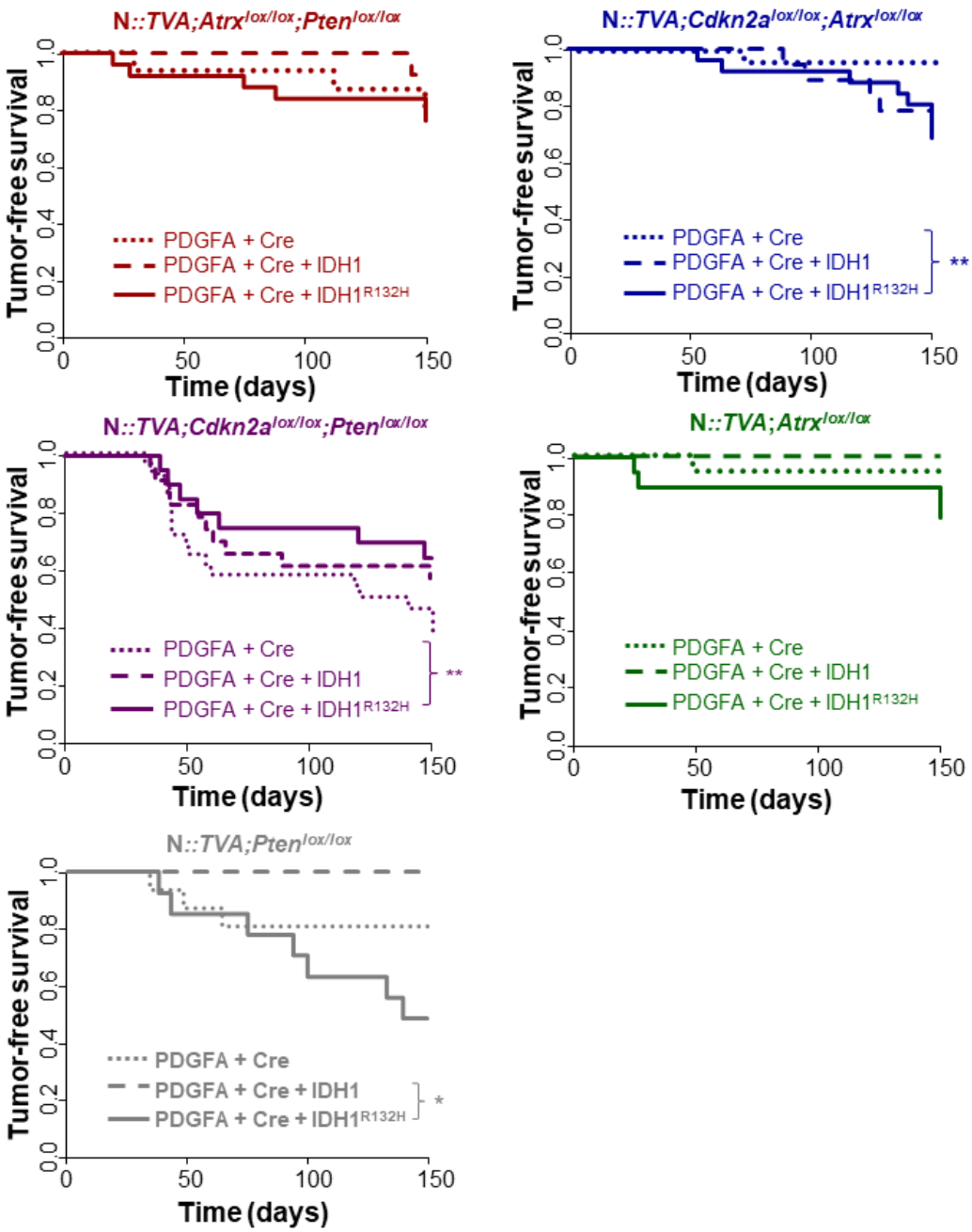

Figure S2. Loss of *Cdkn2a*, *Atrx* and *Pten* cooperate with IDH^{R132H} and PDGFA to promote glioma formation. Related to Figure 2, Table S1, and Table S2. Kaplan-Meier tumor-free survival analysis of the indicated mouse strains (denoted by color) infected with viruses containing PDGFA and Cre (round dotted line), PDGFA, Cre, and wild type IDH1 (dashed line), or PDGFA, Cre, and IDH1^{R132H} (solid line). The number of mice in each cohort is shown in Table S1. Statistical significance is shown by the following key: * $P < 0.05$, ** $P < 0.01$, *** $P < 0.001$. *ns* = not significant.

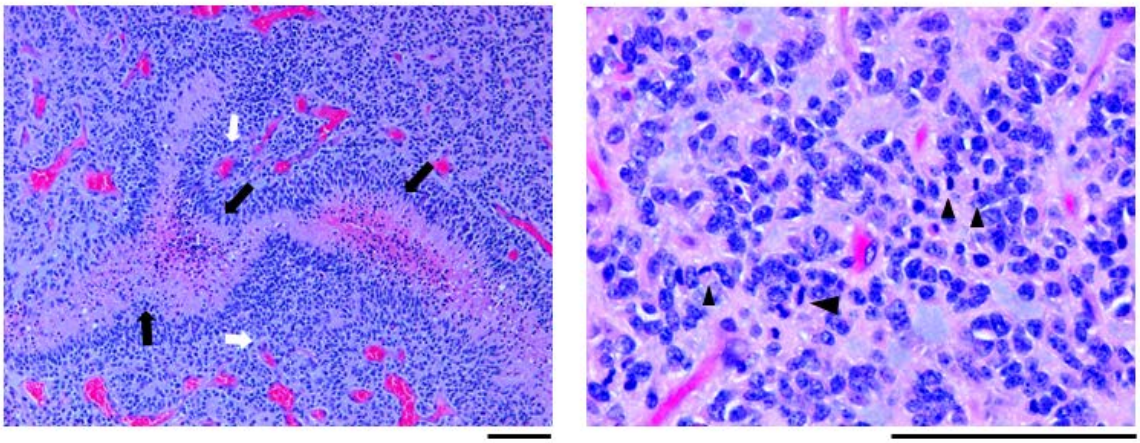

Figure S3. Histological examination of gliomas from N:*:TVA;Cdkn2a*$^{lox/lox}$*;Atrx*$^{lox/lox}$*;Pten*$^{lox/lox}$ mice injected with viruses containing PDGFA, Cre, and IDH1^{R132H}. Related to Figures 3 and S4. Representative H&E images showing features of GBM including pseudopalisading necrosis (black arrows), vascular proliferation (white arrows), and mitotic figures (black arrowheads). Scale bars represent 100 μm.

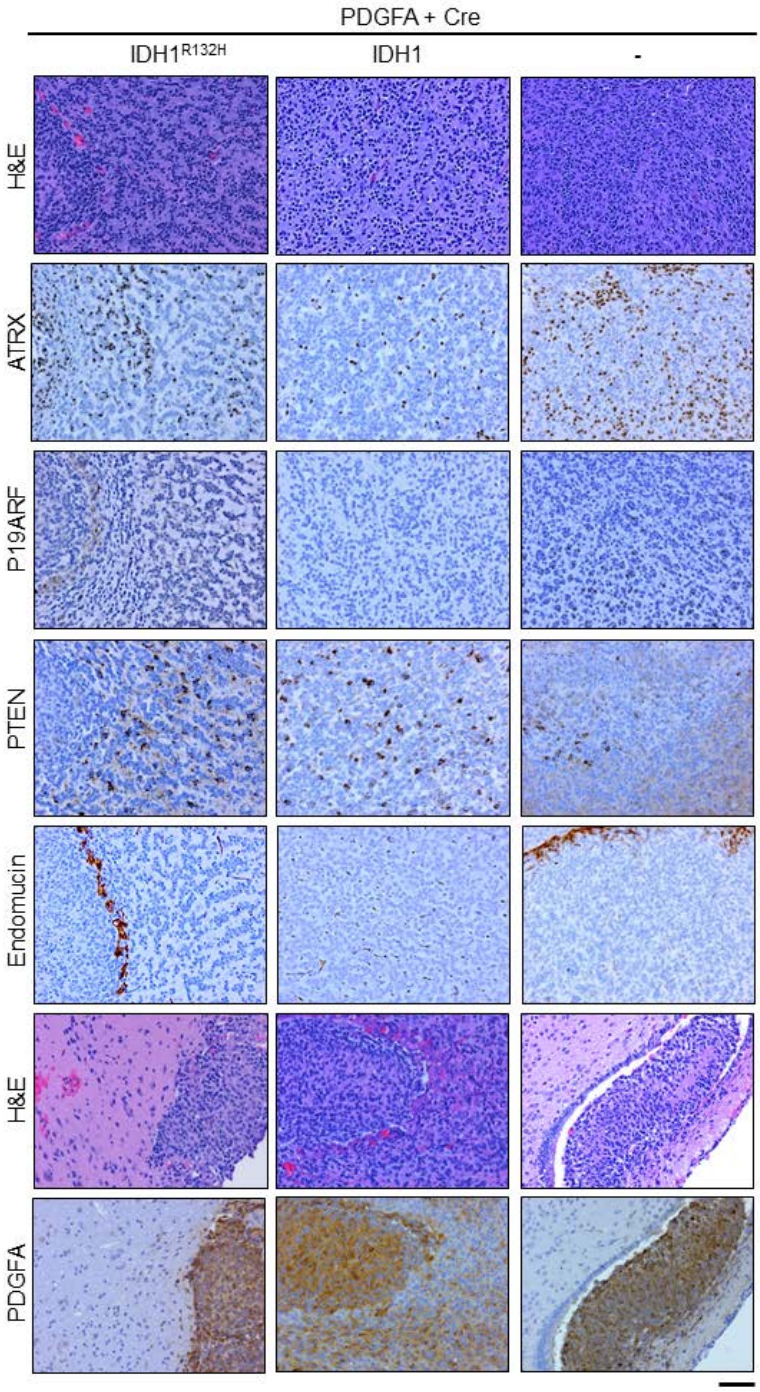

Figure S4. Immunohistochemical staining of gliomas from N::*TVA;Cdkn2a*$^{lox/lox}$*;Atrx*$^{lox/lox}$*;Pten*$^{lox/lox}$ injected mice. Related to Figures 3 and S3. Representative IHC sections of ATRX, P19ARF, PTEN, endomucin, and PDGFA in tumors from each strain of mice injected with viruses containing PDGFA and Cre alone (right column) or in combination with IDH1^{R132H} (left column) or wt IDH1 (middle column) as indicated. Corresponding H&E images are included for reference. Scale bar represents 100 μm.

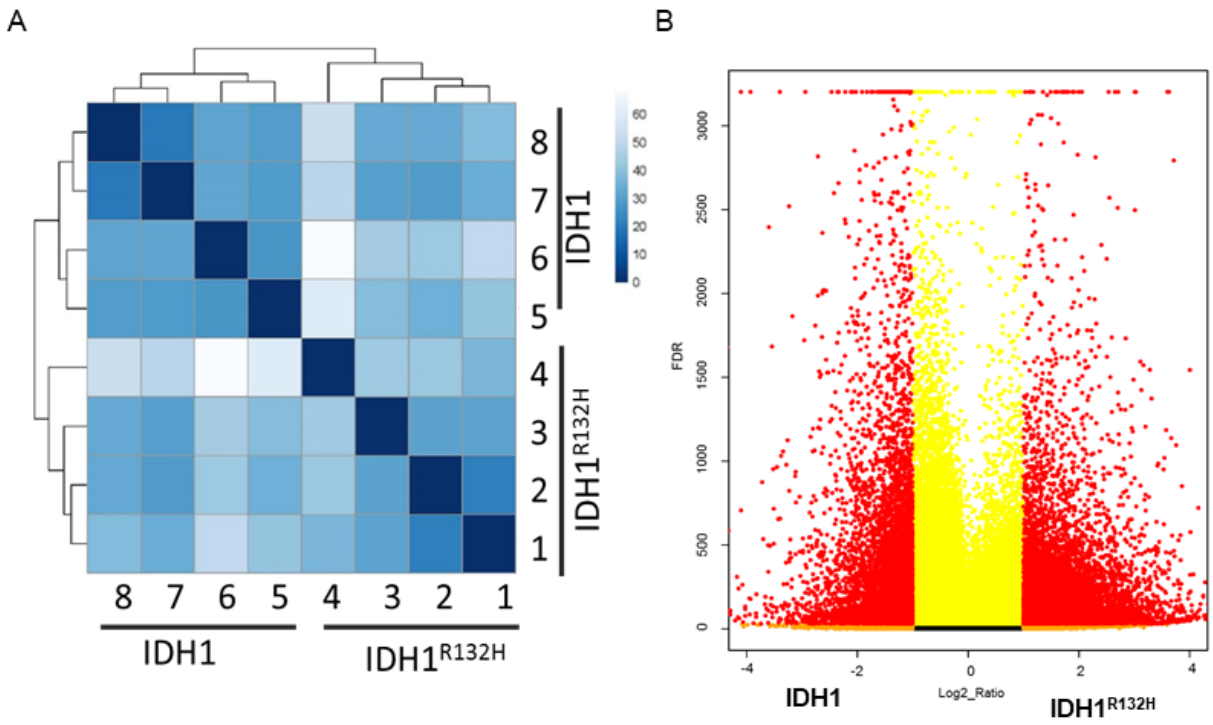

Figure S5. IDH1^{R132H} alters the methylation landscape in mouse gliomas. Related to Figure 6. (A) Heat map showing the relationship between all samples, where values represent a Euclidean distance calculated in R (B) Volcano plot showing differences in DNA methylation between IDH^{1R132H} and IDH1 samples. Each point represents a tested CpG region; points in red pass both significance and fold-change methylation.

Table S1. Tumor incidence by genotype and injection, Related to Figure 2, Figure S2, and Table S2.

Genotype	PDGFA + Cre + IDH^{R132H}	PDGFA + Cre + IDH1	PDGFA + Cre	Cre + IDH^{R132H}
N*::TVA;Atrx*$^{lox/lox}$	4/19(21%)	0/15 (0%)	1/18(5%)	0/4(0%)
N*::TVA;Cdkn2a*$^{lox/lox}$*;Atrx*$^{lox/lox}$	8/25(32%)	4/18(22%)	1/24(4%)	0/28(0%)
N*::TVA;Atrx*$^{lox/lox}$*;Pten*$^{lox/lox}$	6/26(23%)	1/13 (8%)	3/15(20%)	ND
N*::TVA;Cdkn2a*$^{lox/lox}$*;Atrx*$^{lox/lox}$*;Pten*$^{lox/lox}$	14/16(88%)	3/15(20%)	3/15(20%)	0/9(0%)
N*::TVA;Cdkn2a*$^{lox/lox}$*;Pten*$^{lox/lox}$	7/20 (35%)	10/24(42%)	15/29(59%)	0/10(0%)
N*::TVA;Pten*$^{lox/lox}$	7/13 (54%)	0/8(0%)	3/15(20%)	ND

ND: not done

Table S2. Tumor incidence and tumor-free survival by genotype for IDH1^{R132H} and IDH1 cohorts, Related to Figure 2, Figure S2, and Table S1.

Mouse Strain	Gene(s) delivered	Incidence	Median tumor-free survival (days)
N*::TVA;Atrx*$^{lox/lox}$	PDGFA + Cre + IDH1^{R132H}	4/19(21%)	150 ± 9.0
N*::TVA;Cdkn2a*$^{lox/lox}$*;Atrx*$^{lox/lox}$	PDGFA + Cre + IDH1^{R132H}	8/25(32%)	150 ± 5.2
N*::TVA;Atrx*$^{lox/lox}$*;Pten*$^{lox/lox}$	PDGFA + Cre + IDH1^{R132H}	6/26(23%)	150 ± 7.4
N*::TVA;Cdkn2a*$^{lox/lox}$*;Atrx*$^{lox/lox}$*;Pten*$^{lox/lox}$	PDGFA + Cre + IDH1^{R132H}	14/16(88%)	43.5 ± 11
N*::TVA;Cdkn2a*$^{lox/lox}$*;Pten*$^{lox/lox}$	PDGFA + Cre + IDH1^{R132H}	7/20(35%)	150 ± 10
N*::TVA;Pten*$^{lox/lox}$	PDGFA + Cre + IDH1^{R132H}	7/13(54%)	150 ± 12
N*::TVA;Atrx*$^{lox/lox}$	PDGFA + Cre + IDH1	0/15(0%)	150 ± 0.0
N*::TVA;Cdkn2a*$^{lox/lox}$*;Atrx*$^{lox/lox}$	PDGFA + Cre + IDH1	4/18(22%)	150 ± 4.5
N*::TVA;Atrx*$^{lox/lox}$*;Pten*$^{lox/lox}$	PDGFA + Cre + IDH1	1/13(8%)	150 ± 0.5
N*::TVA;Cdkn2a*$^{lox/lox}$*;Atrx*$^{lox/lox}$*;Pten*$^{lox/lox}$	PDGFA + Cre + IDH1	3/15(20%)	150 ± 8.0
N*::TVA;Cdkn2a*$^{lox/lox}$*;Pten*$^{lox/lox}$	PDGFA + Cre + IDH1	10/24(42%)	150 ± 10
N*::TVA;Pten*$^{lox/lox}$	PDGFA + Cre + IDH1	0/8(0%)	150 ± 0.0

References

Almeida, J.S., Iriabho, E.E., Gorrepati, V.L., Wilkinson, S.R., Gruneberg, A., Robbins, D.E., and Hackney, J.R. (2012). ImageJS: Personalized, participated, pervasive, and reproducible image bioinformatics in the web browser. Journal of pathology informatics *3*, 25.

Losman, J.A., Looper, R.E., Koivunen, P., Lee, S., Schneider, R.K., McMahon, C., Cowley, G.S., Root, D.E., Ebert, B.L., and Kaelin, W.G., Jr. (2013). (R)-2-hydroxyglutarate is sufficient to promote leukemogenesis and its effects are reversible. Science *339*, 1621-1625.

Lu, F., Chen, Y., Zhao, C., Wang, H., He, D., Xu, L., Wang, J., He, X., Deng, Y., Lu, E.E., *et al.* (2016). Olig2-Dependent Reciprocal Shift in PDGF and EGF Receptor Signaling Regulates Tumor Phenotype and Mitotic Growth in Malignant Glioma. Cancer cell *29*, 669-683.

Nix, D.A., Di Sera, T.L., Dalley, B.K., Milash, B.A., Cundick, R.M., Quinn, K.S., and Courdy, S.J. (2010). Next generation tools for genomic data generation, distribution, and visualization. BMC bioinformatics *11*, 455.

Robinson, J.P., VanBrocklin, M.W., Guilbeault, A.R., Signorelli, D.L., Brandner, S., and Holmen, S.L. (2010). Activated BRAF induces gliomas in mice when combined with Ink4a/Arf loss or Akt activation. Oncogene *29*, 335-344.

Shin, C.H., Grossmann, A.H., Holmen, S.L., and Robinson, J.P. (2015). The BRAF kinase domain promotes the development of gliomas in vivo. Genes & cancer *6*, 9-18.

Shin, C.H., Robinson, J.P., Sonnen, J.A., Welker, A.E., Yu, D.X., VanBrocklin, M.W., and Holmen, S.L. (2017). HBEGF promotes gliomagenesis in the context of Ink4a/Arf and Pten loss. Oncogene.

Vanbrocklin, M.W., Robinson, J.P., Lastwika, K.J., McKinney, A.J., Gach, H.M., and Holmen, S.L. (2012). Ink4a/Arf loss promotes tumor recurrence following Ras inhibition. Neuro Oncol *14*, 34-42.

Verhaak, R.G., Hoadley, K.A., Purdom, E., Wang, V., Qi, Y., Wilkerson, M.D., Miller, C.R., Ding, L., Golub, T., Mesirov, J.P., *et al.* (2010). Integrated genomic analysis identifies clinically relevant subtypes of glioblastoma characterized by abnormalities in PDGFRA, IDH1, EGFR, and NF1. Cancer cell *17*, 98-110.